# Proto-monsoon rainfall and greening in Central Asia due to extreme early Eocene warmth

Niels Meijer, Alexis Licht, Amber Woutersen, Carina Hoorn, Faez Robin-Champigneul, Alexander Rohrmann, Mattia Tagliavento, Julia Brugger, Fanni Kelemen, Andrew Schauer, et al.

## ▶ To cite this version:

Niels Meijer, Alexis Licht, Amber Woutersen, Carina Hoorn, Faez Robin-Champigneul, et al.. Proto-monsoon rainfall and greening in Central Asia due to extreme early Eocene warmth. Nature Geoscience, 2024, 17 (2), pp.158-164. 10.1038/s41561-023-01371-4 . hal-04426859

**HAL Id: hal-04426859**
**https://hal.science/hal-04426859**

Submitted on 30 Jan 2024

# Proto-monsoon rainfall and greening in Central Asia due to extreme early Eocene warmth

Niels Meijer[1], Alexis Licht[2], Amber Woutersen[3], Carina Hoorn[3], Faez Robin-Champigneul[4], Alexander Rohrmann[5], Mattia Tagliavento[6], Julia Brugger[1], Fanni D. Kelemen[7], Andrew J. Schauer[8], Micheal T. Hren[9], Aijun Sun[10-12], Jens Fiebig[6], Andreas Mulch[1,6], Guillaume Dupont-Nivet[13,14]

1) Senckenberg Biodiversity and Climate Research Centre (SBiK-F), Frankfurt am Main, Germany.
2) CNRS, IRD, INRAE, CEREGE, Aix Marseille University, Aix-en-Provence, France.
3) Department of Ecosystem and Landscape Dynamics (ELD), Institute for Biodiversity and Ecosystem Dynamics (IBED), University of Amsterdam, Amsterdam, the Netherlands.
4) Maastricht University, Faculty of Science and Engineering, Maastricht Science Programme, Maastricht, the Netherlands.
5) Institute of Geological Sciences, Freie Universität Berlin, Berlin, Germany
6) Goethe University Frankfurt, Institute of Geosciences, Frankfurt am Main, Germany.
7) Goethe University Frankfurt, Institute for Atmospheric and Environmental Sciences, Frankfurt am Main, Germany.
8) Department of Earth and Space Sciences, University of Washington, Seattle, WA, USA.
9) Department of Earth Sciences, University of Connecticut, Storrs, CT, USA
10) Key Laboratory of Western China's Environmental Systems (Ministry of Education), College of Earth and Environmental Sciences, Lanzhou University, Lanzhou, China.

11) Key Laboratory of Desert and Desertification, Northwest Institute of Eco-Environment
and Resources, Chinese Academy of Sciences, Lanzhou, China.
12) University of Chinese Academy of Sciences, Beijing, China.
13) Géosciences Rennes-UMR CNRS 6118, Univ Rennes, CNRS, Rennes, France.
14) GFZ German Research Centre for Geosciences, Potsdam, Germany

**The dry continental interior of Asia has remained arid throughout most of its geological history, yet the future of this unique ecosystem remains unclear. Here, we use palynological and isotopic records to track vegetation and moisture throughout the warm early Eocene (57 to 44 million years ago) as an analogue for extreme atmospheric $CO_2$ scenarios. We show that rainfall temporarily doubled and replaced the regional steppe by forested ecosystems. By reconstructing the season of pedogenic carbonate growth we constrain the soil hydrologic regime and show that most of this rainfall occurred during the summer season. This humid event is therefore attributed to an inland expansion of monsoonal moisture following the massive greenhouse gas release of the Paleocene-Eocene Thermal Maximum (PETM) as identified by a negative carbon isotope excursion. The resulting abrupt greening of the Central Asian steppe-desert would have enabled mammal dispersal and could have played a role in carbon cycle feedbacks by enhancing soil organic carbon burial and silicate weathering. These extreme Eocene proto-monsoons, albeit different from the topography-driven Asian monsoon today, highlight the potential for abrupt shifts in Central Asian rainfall and ecosystems under future global warming.**

The vast Asian continental interior is home to a unique and diverse steppe-desert biome that has existed for millions of years[1], yet its hydroclimatic future and response to extreme atmospheric $CO_2$ concentrations ($pCO_2$) remains poorly understood[2]. Sedimentary archives of past warming events together with climate model simulations provide valuable insights[3], especially regarding the Eocene period (56-34 Ma) which was characterized by short-lived hyperthermal events of abrupt warming[4,5]. The largest and most pronounced of these is the Paleocene-Eocene Thermal Maximum (PETM; 56 Ma) lasting several 10 ka, during which $pCO_2$ reached more than 6× the pre-industrial atmospheric $CO_2$ concentration[6-8]. Records of such hyperthermal events affecting inland Asia are rare and hard to decipher because we commonly lack unambiguous rainfall proxies with respect to the various regional moisture sources, thereby limiting our understanding of the hydroclimatic response to climate forcing, including future projections under higher $pCO_2$[3].

The scarce precipitation reaching inland Asia today mostly originates from monsoons during summer or the mid-latitude westerlies during winter to spring (Fig. 1 A; Extended Data Fig. 1)[9,10]. Paleoclimate models and geological records indicate that growth of the Tibetan-Himalayan orogen and retreat of the Paratethys Sea modulated monsoons and westerlies since the Eocene (Fig. 1 A)[11-14]. Proto-monsoons existed already before significant surface uplift of the Tibetan Plateau, but it remains debated whether these were similar to today[15-17], less intense[18] or only restricted to the tropical low latitudes[13,14,19] except during extreme orbital conditions[20,21]. Eocene paleobotanical data show that summer monsoons transported abundant precipitation to the East Asian coast[17,22], while regional soil respiration derived from carbon isotope ratios ($\delta^{13}C$) of pedogenic carbonates suggest that monsoons may have reached further inland[10]. Oxygen isotope ratios ($\delta^{18}O$) on the other hand, suggest that the mid-latitude westerlies provided winter to springtime precipitation to Central Asia, especially before the Neogene surface uplift of the Tien Shan and Pamir mountains, which block most of this moisture today[9,10,23]. However, the isotopic composition of this westerly precipitation is difficult to distinguish from summer monsoonal moisture reaching the continental interior[10].

Key in distinguishing between these different Asian moisture regimes is therefore to identify not only the isotopic composition and amount of precipitation, but also the seasonal timing, which remains difficult to assess from geological records. Here, we address this issue using a novel approach of combining fossil sporomorphs (pollen and spores) and soil organic matter as proxy for precipitation[24] together with clumped isotope ($\Delta_{47}$) temperatures of co-occurring pedogenic carbonates which mostly form during the dry season[25,26]. By comparing these $\Delta_{47}$-derived soil temperatures with seasonal climate model estimates we distinguish whether soil dewatering occurred predominantly during a winter-time dry season after a wet summer monsoon, or during summer drying of westerly-derived soil moisture[27,28]. Today, the monsoons and westerlies meet along the northeastern margin of the Tibetan Plateau, which includes the continental Xining Basin (China) and is ideally located to track the evolution of these moisture sources (Fig. 1). Previous soil temperature reconstructions throughout the middle Eocene and Oligocene show that the Xining Basin was at low elevation[27], while steppe-desert pollen, presence of evaporites and reduced soil respiration indicate aridity[1,23,29]. Dating of this sedimentary record has now been extended to the early Eocene based on magnetostratigraphy and radiometric ages[23,30] allowing us to investigate the Central Asian steppe response to hyperthermal conditions.

## Increased rainfall during a carbon isotope excursion

Early Eocene hyperthermals were driven by the periodic injection of greenhouse gases into the atmosphere from low-$\delta^{13}C$ reservoirs. This resulted in negative carbon isotope excursions (CIE) across the globe that have been detected in various terrestrial proxies such as plant waxes ($\delta^{13}C_{wax}$ of $C_{29}$ to $C_{31}$ *n*-alkanes) or bulk soil organic matter ($\delta^{13}C_{SOM}$)[6]. In the Xining Basin, $\delta^{13}C$ values are relatively high throughout most of the Eocene, but we identify an abrupt and large CIE of -6‰ in $\delta^{13}C_{SOM}$ and -8‰ in compound specific $\delta^{13}C_{wax}$ (Fig. 2). This is significantly larger than the CIEs related to early Eocene hyperthermals which typically attain magnitudes of up to -4‰[4,5], but very similar in both shape and magnitude to continental records of the PETM[6,32,33].

The Xining CIE is preceded by alluvial mudflat deposits at the basin margin (Ledu section) and organic-rich gypsum in the basin center (Bingling Shan and Caijia sections) indicating dry conditions. This is corroborated by the predominance of steppe-desert shrubs in the palynological record and high $\delta^{13}C$ values which today are only found in extremely dry ecosystems[24,34] (Fig. 2). The negative CIE starts abruptly in the uppermost gypsum bed and spans ~30 meters into the overlying organic-rich alluvial mudflat deposits[30]. Steppe-desert pollen decrease during this interval and the vegetation becomes dominated by temperate forests and ferns indicating a shift to wetter conditions. Less water stress experienced by C3 vegetation and the corresponding shift in biome typically results in lower $\delta^{13}C$ values[34,35]. If combined with a dramatic drop of atmospheric carbon isotopic composition ($\delta^{13}C_{atm}$), such as seen during hyperthermals[6,35,36], these ecological changes could produce the large size of the CIE observed in the Xining Basin.

Organic matter recorded in soils provides a natural average of the aboveground biomass and can be used to reconstruct the amount of rainfall when corrected for changes in $\delta^{13}C_{atm}$ (Fig. 2 and Extended Data Fig. 2)[24]. Even when assuming an extreme change of $\delta^{13}C_{atm}$ such as observed during the PETM[6,35], reconstructed mean annual precipitation (MAP) values suggest at least a doubling of MAP in the Xining Basin during the CIE (~574 mm/year) compared to the evaporites below (~177 mm/year). Using the $\delta^{13}C_{atm}$ value of lower magnitude Eocene hyperthermals would result in an even larger increase in MAP (~984 mm/year) and using the early Eocene baseline value would imply an unrealistic MAP of >4000 mm/year (Supplementary Data 4). Throughout the remainder of the Eocene Xining record, $\delta^{13}C_{SOM}$ values remain relatively high[29] indicating aridity which fits the predominant redbeds, evaporites and steppe-desert shrubs observed in the record[1,23]. The CIE in the Xining Basin is thus a unique window where both palynological assemblages and $\delta^{13}C$ values show a significant greening of the otherwise arid Asian interior. In the following, we will use soil carbonates to test whether this greening was driven by increased westerly moisture or monsoons (Fig. 1).

## Clumped isotope evidence for summer rainfall

Well-developed pedogenic carbonate nodules are rare in the Xining Basin record but were identified in three horizons of the Ledu section. In consequence, the carbonate component of the alluvial mudrocks was assessed as well using Scanning Electron

Microscopy (SEM), X-Ray Diffraction (XRD; Fig. 2; Extended Data Fig. 3) and both optical and cathodoluminescence (CL) microscopy (Extended Data Fig. 4). The strata between 50 Ma and 45 Ma contain mostly calcian dolomite (6-20%), while the intervals above and below are dominated by calcite (1-14%). This calcite is mostly dull luminescent micrite and is interpreted as vadose-grown cement with no evidence of phreatic overprinting (Extended Data Fig. 4 A and B). These cements precipitate either from rising shallow groundwater or percolating soil water and are similar to pedogenic carbonates[37]. In contrast, the calcian dolomite may have formed either by syn-sedimentary precipitation from saline brines or late diagenetic replacement of calcite cements[38]. Hence, we focus our isotope investigations solely on the vadose-grown calcite and micritic pedogenic nodules (Extended Data Fig. 4 C) to avoid diagenetic overprinting.

Clumped isotope thermometry measures the relative abundance of calcite-derived $CO_2$ isotopologues of mass 47 compared to the predicted stochastic distribution ($\Delta_{47}$). Since the bonding between the heavy isotopes ($^{13}C$-$^{18}O$) is temperature-dependent, this measurement allows reconstructing soil temperatures at the time of carbonate growth without prior knowledge of the isotopic composition of the soil water[39]. Most Holocene pedogenic carbonates provide $\Delta_{47}$ temperatures that are warmer than mean annual temperatures (MAT) because intense soil dewatering and carbonate formation is typically biased towards the summer season[25,26]. So far, the only location where soil $\Delta_{47}$ temperatures have systematically yielded winter temperatures is the monsoonal tropical domain, where winters are dry and warm enough for the accumulation of pedogenic carbonates while summers are typically too wet[28]. Colder-than-MAT $\Delta_{47}$ temperatures can thus be interpreted as a signature for a summer rainy season, especially during Eocene times when winter temperatures were overall warmer, facilitating carbonate growth in the winter[28].

Overall, the pedogenic and vadose-grown carbonates in the Xining strata show a wide spread of $\Delta_{47}$ temperatures ranging from 9 ±3 °C to 38 ±4°C (Fig. 2). This range could be due to high evaporative demand throughout the year, resulting in soil drying shortly after erratic rainfall events under variable temperature conditions[26]. In contrast, the $\Delta_{47}$ temperatures during the wetter CIE interval (Fig. 2) are remarkably stable at 20±3°C and surprisingly low, especially given the hyperthermal conditions. When compared with simulated temperatures in the Xining Basin from the various climate models of the Deep-Time Model Intercomparison Project (DeepMIP)[40] these simulated temperatures indicate that carbonate growth during the CIE was biased towards the colder winter months (Fig. 3 A). Especially when considering that the soil temperature might have been 1-4°C warmer than the simulated surface air because of ground heating effects[41].

The $\Delta_{47}$ temperatures during the CIE therefore suggest that soil drying in the Xining Basin occurred during the winter season, while the increased rainfall recorded in the palynological assemblage and $\delta^{13}C$ values must have occurred mostly during the summer. This is similar to the modern monsoonal setting in which pedogenic carbonates near Xining are formed during the fall and after the wet season[42]. Reconstructed soil water $\delta^{18}O$ (-6 ± 1.5‰; Extended Data Fig. 5 and 6) is similar to coeval records of both summer monsoonal and westerly moisture in the region[10], but the cold $\Delta_{47}$ temperatures in combination with increased MAP indicate an intensification of summer monsoons deep within the Asian continent shifting the timing of carbonate formation to the winter season. Cold $\Delta_{47}$ temperatures are not unique to the CIE and reappear episodically in the Xining Basin ~10 million years later and persist into the Oligocene (Fig. 3 A), possibly due to the combined effects of global cooling and an increased role for summer monsoonal moisture[27]. However, the palynological records show that the region remained extremely dry throughout the late Eocene to Oligocene[1] and unlike the intensified monsoon seen during the CIE (Fig. 2).

## Proto-monsoon intensification in hyperthermal conditions

The simulated temperatures fit well with global proxy compilations[43] and the climate models show mutual agreement[40] (Fig 3 A), however, differences between models are large for simulated precipitation[3] (Fig. 3 B). The ‘drier’ models show aridity in the Xining Basin throughout the year (e.g. COSMOS and IPSL), while the ‘wetter’ models reveal a summer rainy season (e.g. CESM and HadCM3) not unlike pre-industrial conditions (Extended Data Fig. 1). Simulated MAP is relatively low and ranges from 25 to 469 mm/year (Fig. 3 B), which fits with the inland evaporative basins in the region[44] and our proxy estimates for the Paleocene and Eocene background conditions in the Xining Basin. However, even the ‘wetter’ simulations are lower than our reconstructed MAP of 574 mm/year for the intensified monsoon during the CIE.

The distribution of monsoonal domains[45] in the simulations shows that the East Asian monsoon was less prevalent in the Eocene compared to today (Fig. 4; Extended Data Fig. 7) and that southern Asia was influenced by the Intertropical Convergence Zone (ITCZ) as suggested by paleobotanical data[19]. Intriguingly, some of the Eocene simulations also show a monsoonal domain along the East Asian coast (CESM, COSMOS and GFDL), in particular in the 6x and 9x $pCO_2$ simulations, which would have resembled the early Eocene atmosphere[8] (Fig. 4; Extended Data Fig. 7). This East Asian proto-monsoon agrees well with paleobotanical compilations showing a humid coast line[17,22], but none of the DeepMIP models reproduce monsoons extending far into the continental interior to reach the Xining Basin.

Other modeling studies have shown that Eocene monsoons can be triggered in extreme orbital settings with amplified northern hemisphere heating[20,21]. The PETM and other hyperthermal events correspond to high eccentricity[7] and these unique conditions combined with extreme greenhouse warming likely conspired to intensify the proto-monsoons to reach the continental interior of Asia. The shape, large magnitude and thickness of the Xining CIE, and its occurrence within a long reversed polarity zone correlated with chron C24r (57.1 Ma to 53.9 Ma) allow us to attribute the CIE to the PETM (56 Ma), which also fits within the radiometric age constraints (Fig. 2; Extended Data Fig. 8). Alternatively, it could be ETM2 (54 Ma) but this hyperthermal is considerably smaller in size, shorter and consists of two excursions (H1 and H2) that have been observed in both marine and terrestrial records[4,5,32] but are absent in the Xining Basin. Furthermore, negative CIEs with a shape and size similar to the Xining CIE have been observed in the continental Nanyang and Fushun Basins in eastern China and are also linked to reduced water stress during the PETM[36]. As the largest hyperthermal, the PETM is therefore the most likely driver for this unique event of monsoon intensification and greening in Central Asia.

Finally, we note that the Eocene proto-monsoons were significantly different from the modern-day East Asian monsoon, which is mostly driven by interaction between the subtropical jet stream and the high topography of the Tibetan Plateau[12]. Eocene proto-monsoons occur even in the DeepMIP simulations with no Tibetan Plateau at all (Fig. 4) and are driven by a distinct low atmospheric pressure anomaly developing during summer over the vast and flat Asian continent (Extended Data Fig. 9). This suggests that the proto-monsoons were similar to a large sea breeze driven by land-sea thermal contrasts[18] and explains their sensitivity to hyperthermal conditions. Global cooling after the early Eocene reduced regional thermal contrasts, dampening the ability of proto-monsoons to episodically expand inland and could explain the overall aridification trend of Central Asia throughout the Eocene and culminating at the Eocene-Oligocene Transition (EOT; 33.9 Ma)[27,29,46]. Only until the subsequent surface uplift and northward expansion of the Tibetan Plateau during the Neogene would the modern-day East Asian monsoon have returned to the Xining Basin and the Asian interior[11-14].

Our study thus reveals a prominent role for Eocene proto-monsoons in occasionally greening the otherwise dry Asian interior under hyperthermal conditions. The PETM, but also other hyperthermals such as the Middle Eocene Climatic Optimum (MECO) are associated with major mammal dispersals in and out of Asia[47,48] and future work should consider the role of proto-monsoons in shifting biomes[49] and opening dispersal corridors within continental Asia. Replacing the steppe-desert by forested ecosystems could have also played a major role in buffering the massive carbon release during hyperthermals by enhancing soil organic carbon burial and silicate weathering[50]. Finally, our work provides paleoclimate evidence highlighting the abrupt and non-linear response of Asian monsoons to extreme greenhouse warmth. Although the Eocene Asian paleogeography and hydroclimate were markedly different from today, the mechanisms leading to abrupt greening of the Asian interior should be further tested and simulated because of their significance for predicting future rainfall patterns.

## Acknowledgments

This study was funded by an ERC consolidator grant (MAGIC 649081 to GDN) and through the VeWA consortium by the LOEWE programme of the Hessen Ministry of Higher Education, Research and the Arts, Germany. We thank Rainer Petschick for help with the XRD analyses as well as Jeremy McCormack and Amelia Davies for suggestions on the formation of dolomite. We acknowledge Roy Erkens and the following students from Maastricht University for their help in exploring the palynological samples:  Henry del Marmol, Lucas Sauerschnig, Kaatje de Jong, Amaia Villagrasa, Lael Licht, Henry de Schrevel, and Benedetto Diana. We also acknowledge Hanna van den Hill (University of Amsterdam) and Julia Gravendeyk (University of Bonn) for extensive sporomorph documentation. We thank Hanno Meyer for kindly providing organic stable isotope analyses and Armelle Ballian, Sven Hofmann and Simon Anderson for assistance with stable and clumped isotope analyses. We also thank Christina Günter and Uwe Altenberger for their help with the SEM and CL. We are grateful to Natasha Barbolini, Xiang-Jun Liu, Xiaohui Wu, Zhipeng Wu, Meimei Xiao and Yang Zhang for their support with collecting the samples. We also acknowledge the efforts of the DeepMIP community and are thankful for the available climate model simulation data.

## Author contributions

N.M., A.L. and G.D.-N. designed the study. N.M., A.L., A.W., A.R., A.S. and G.D.-N. conducted the field work and collected the samples. N.M. performed the XRD and petrographic analyses. A.W., F.R.-C. and C.H. prepared and analysed the palynological samples. A.R. and M.T.H. performed the *n*-alkane analyses. N.M., A.L., A.J.S. and A.M. conducted the stable isotope analyses. N.M., M.T. and J.F. performed the clumped isotope analyses. J.B. and F.D.K. analysed and plotted the climate model simulation data. N.M. wrote the manuscript with major input from A.L., G.D.-N. and A.M. All co-authors contributed to interpreting the data and writing the manuscript.

## Competing Interests Statement

The authors declare no competing interests.

## Figures

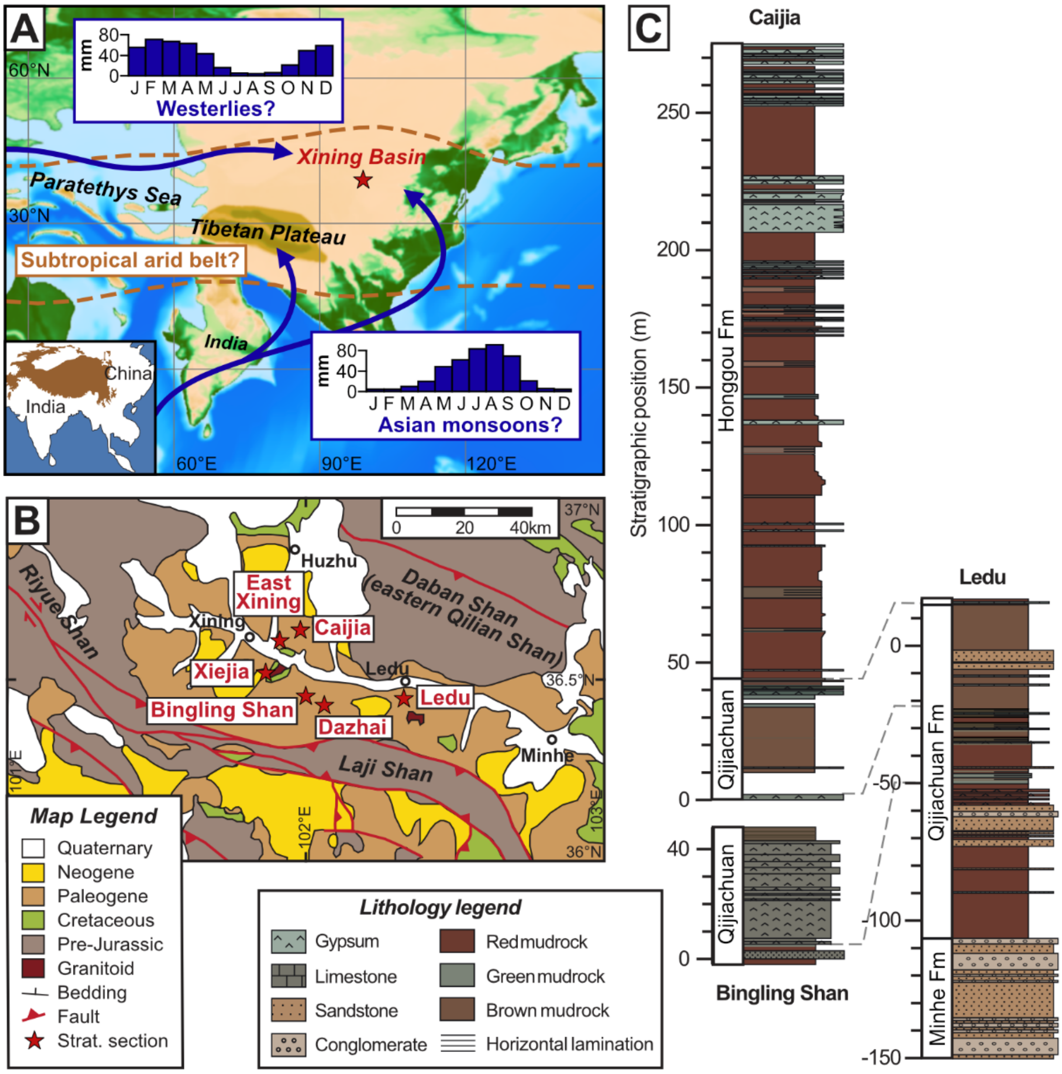

*Fig. 1. Geological setting showing hypothesized Eocene hydroclimates in Asia including a subtropical arid belt, westerly or monsoonal domain. A) Paleogeographic map of Asia at 50 Ma (million years ago)[31] showing the location of the Xining Basin. Blue arrows show potential moisture sources. Histograms reflect the seasonal distribution of this rainfall based on modern-day observations in monsoonal Xining and westerly-dominated Tashkent (https://www.ncei.noaa.gov/products/wmo-climate-normals). Climate model simulations indicate a similar seasonal distribution of rainfall in these domains during the Eocene[9,20]. Inset shows present-day geographical location. B) Geological map of the Xining Basin (modified from ref[30]) showing the*

*locations of the studied sections and palynological sampling. C) Lithostratigraphy of the Caijia, Bingling Shan and Ledu key sections[23,30].*

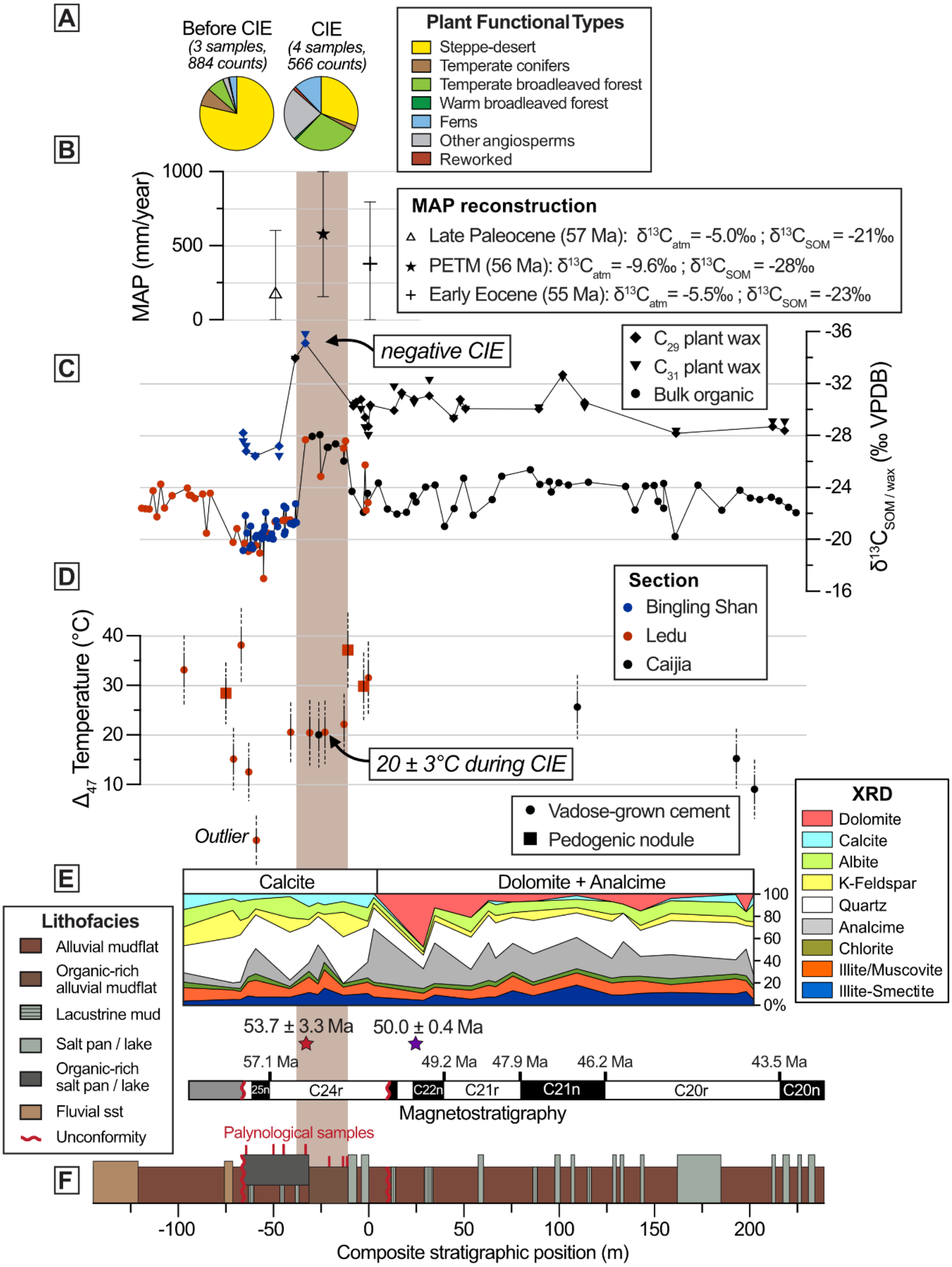

*Fig. 2. Paleo-environmental reconstruction showing temperate forests replacing steppe shrubs during a negative carbon isotope excursion (CIE). The CIE is indicated by the brown shaded vertical bar. Data include: A) palynological data classified in Plant Functional Types, B) reconstructed Mean Annual Precipitation (MAP) using late Paleocene, PETM and early Eocene* $\delta^{13}C_{atm}$ *and* $\delta^{13}C_{SOM}$ *values (root mean square error of ±422 mm/year of the MAP proxy is shown)*[24]*, C)* $\delta^{13}C$ *values of both soil organic matter and n-alkanes, D)* $\Delta_{47}$ *temperatures of vadose-grown carbonates (with solid and dashed lines indicating 68% and 95% confidence intervals respectively based on at least 13 replicates), one sample produced an unrealistically low temperature of -1.3°C and is considered an outlier, E) X-Ray Diffraction (XRD) derived mineral content, F) age constraints*[23,30] *based on radiometric ages (stars) and magnetic polarities (black ticks), lithostratigraphy showing stratigraphic positions of palynological samples with red marks.*

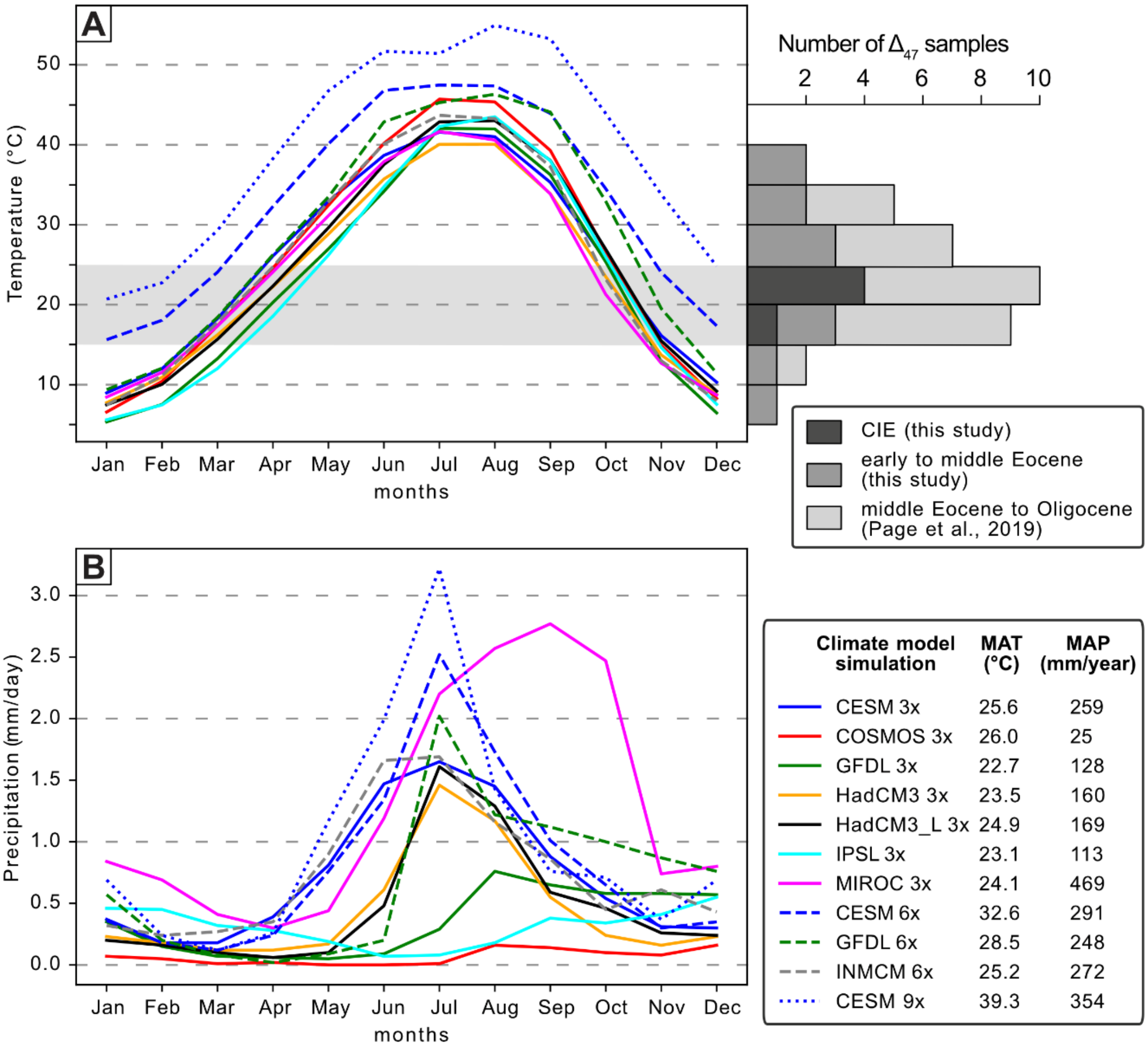

*Fig. 3. Proxy comparison with simulated surface air temperature (A) and precipitation (B) in the Eocene Xining Basin. Averaged values were derived from a box of 1.875° latitude by 2.5° longitude centred at the paleolocation of the Xining Basin (102.5°N, 39.5°E). Simulations are derived from the DeepMIP climate model ensemble (colors indicate each model) under an early Eocene paleogeography with no Tibetan Plateau and a Paratethys Sea lowstand, preindustrial orbital configuration and 3x, 6x or 9x preindustrial pCO*$_2$ *when available (solid, dashed and dotted lines respectively)*[40]*. The histogram in A) shows the number of measured* $\Delta_{47}$ *temperatures in 5°C bins. CIE temperatures of ~20°C are best explained by soil dewatering and carbonate formation*

*during the colder winter months. Simulated precipitation in B) varies from dry throughout the year to summer wet similar to the present-day monsoons.*

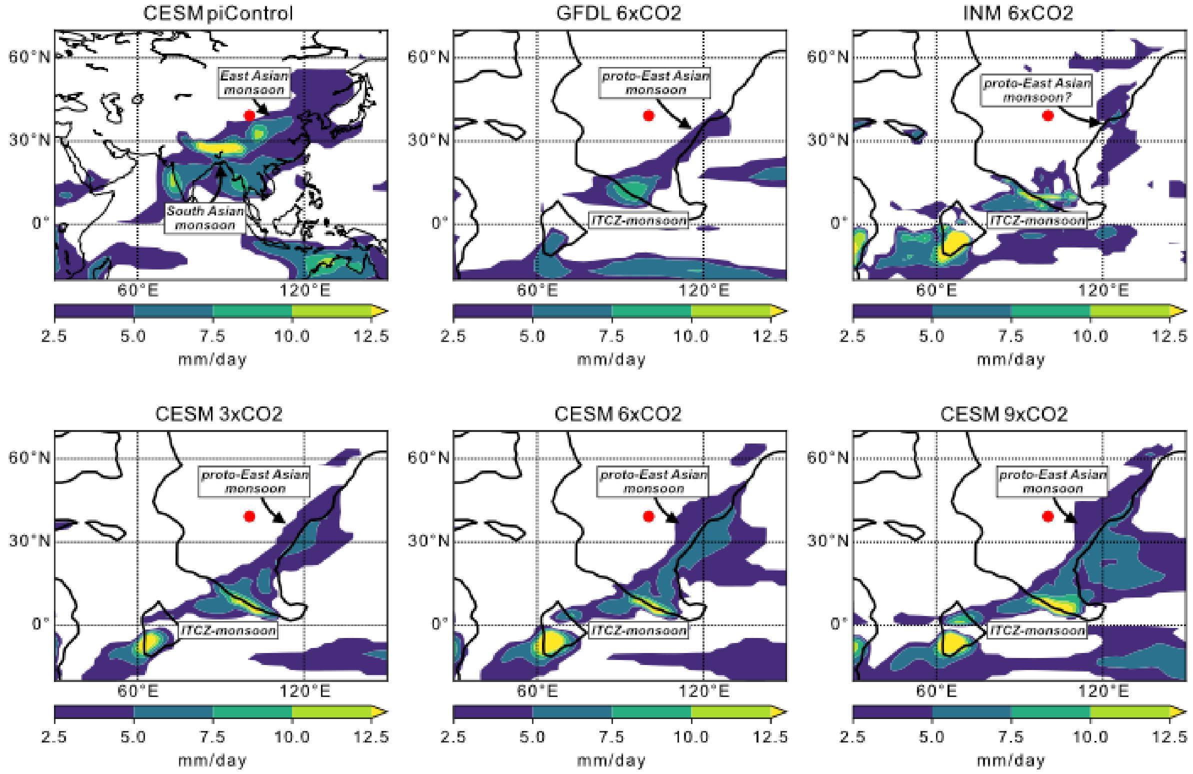

*Fig. 4. Distribution of monsoonal domains in climate model simulations. Upper panel shows a pre-industrial control simulation (CESM) and two early Eocene simulations with 6x $pCO_2$ (GFDL and INM). Lower panel shows different $pCO_2$ scenarios (3x, 6x and 9x) of the CESM model. Additional simulations are shown in Extended Data Fig. 7. Summer (MJJAS) minus winter precipitation (NDJFM) is used as a metric and regions where this difference is >2.5 mm/day are considered monsoonal[45]. Red dot indicates the location of the Xining Basin. All Eocene simulations show an ITCZ (Intertropical Convergence Zone) monsoon near the equator. CESM and GFDL show a proto-monsoonal domain along the East Asian coast, but none of the models simulate monsoons extending far into the Asian interior.*

## References

1. Barbolini, N., Woutersen, A., Dupont-Nivet, G., Silvestro, D., Tardif, D., Meijer, N., Chang, C., H.-X. Zhang, A. Licht, Rydin, C., Koutsondendris, A., Han, F., Rohrmann, A., Liu, X.-J., Zhang, Y., Donnadieu, Y., Fluteau, F., Ladant, J.-B., Le Hir, G., Hoorn, C. (2020). Cenozoic evolution of the steppe-desert biome in Central Asia. Science Advances, 6(41), eabb8227. https://doi.org/10.1126/sciadv.abb8227
2. Li, C., Fu, B., Wang, S., Stringer, L. C., Wang, Y., Li, Z., Liu, Y. & Zhou, W. (2021). Drivers and impacts of changes in China's drylands. *Nature Reviews Earth & Environment*, *2*(12), 858-873. https://doi.org/10.1038/s43017-021-00226-z
3. Cramwinckel, M. J., Burls, N. J., Fahad, A. A., Knapp, S., West, C. K., Reichgelt, T., Greenwood, D. R., Chan, W.-L., Donnadieu, Y., Hutchinson, D. K., de Boer, A. M., Ladant, J.-B., Morozova, P. A., Niezgodzki, I., Knorr, G., Steinig, S., Zhang, Z., Zhu, J., Feng, R., Lunt, D. J., Abe-Ouchi, A. & Inglis, G. N. (2023). Global and zonal-mean hydrological response to early Eocene warmth. Paleoceanography and Paleoclimatology, e2022PA004542. https://doi.org/10.1029/2022PA004542
4. Westerhold, T., Marwan, N., Drury, A. J., Liebrand, D., Agnini, C., Anagnostou, E., Barnet, J. S. K., Bohaty, S. M., De Vleeschouwer, D., Florindo, F., Frederichs, T., Hodell, D. A., Holbourn, A. E., Kroon, D., Lauretano, V., Littler, K., Lourens, L. J., Lyle, M., Pälike, H., Röhl, U., Tian, J., Wilkens, R. H., Wilson, P. A., Zachos, J. C. (2020). An astronomically dated record of Earth's climate and its predictability over the last 66 million years. Science, 369(6509), 1383–1387. https://doi.org/10.1126/scien ce.aba6853

5. Abels, H. A., Lauretano, V., Van Yperen, A. E., Hopman, T., Zachos, J. C., Lourens, L. J., Gingerich, P. D. & Bowen, G. J. (2016). Environmental impact and magnitude of paleosol carbonate carbon isotope excursions marking five early Eocene hyperthermals in the Bighorn Basin, Wyoming. Climate of the Past, 12(5), 1151-1163. https://doi.org/10.5194/cp-12-1151-2016, 2016
6. McInerney, F. A., & Wing, S. L. (2011). The Paleocene-Eocene Thermal Maximum: A perturbation of carbon cycle, climate, and biosphere with implications for the future. Annual Review of Earth and Planetary Sciences, 39, 489-516. https://doi.org/10.1146/annurev-earth-040610-133431
7. Zeebe, R. E., & Lourens, L. J. (2019). Solar System chaos and the Paleocene–Eocene boundary age constrained by geology and astronomy. Science, 365(6456), 926-929. https://doi.org/10.1126/science.aax0612
8. Rae, J. W., Zhang, Y. G., Liu, X., Foster, G. L., Stoll, H. M., & Whiteford, R. D. (2021). Atmospheric CO2 over the past 66 million years from marine archives. Annual Review of Earth and Planetary Sciences, 49, 609-641. https://doi.org/10.1146/annurev-earth-082420-063026
9. Bougeois, L., Dupont-Nivet, G., de Rafélis, M., Tindall, J. C., Proust, J. N., Reichart, G. J., de Nooijer, L. J., Guo, Z. & Ormukov, C. (2018). Asian monsoons and aridification response to Paleogene sea retreat and Neogene westerly shielding indicated by seasonality in Paratethys oysters. Earth and Planetary Science Letters, 485, 99-110. https://doi.org/10.1016/j.epsl.2017.12.036
10. Caves Rugenstein, J. K., & Chamberlain, C. P. (2018). The evolution of hydroclimate in Asia over the Cenozoic: A stable-isotope perspective. Earth-

Science Reviews, 185, 1129-1156. https://doi.org/10.1016/j.earscirev.2018.09.003

11. An, Z., Kutzbach, J. E., Prell, W. L., & Porter, S. C. (2001). Evolution of Asian monsoons and phased uplift of the Himalaya–Tibetan plateau since Late Miocene times. Nature, 411(6833), 62. https://doi.org/10.1038/35075035
12. Molnar, P., Boos, W.R., Battisti, D.S. (2010). Orographic controls on climate and paleoclimate of Asia: thermal and mechanical roles for the Tibetan Plateau. Annu. Rev. Earth Planet. Sci.38. https://doi .org /10 .1146 /annurev-earth -040809 -152456.
13. Sun, X., & Wang, P. (2005). How old is the Asian monsoon system?—Palaeobotanical records from China. Palaeogeography, Palaeoclimatology, Palaeoecology, 222(3-4), 181-222. https://doi.org/10.1016/j.palaeo.2005.03.005
14. Wu, F., Fang, X., Yang, Y., Dupont-Nivet, G., Nie, J., Fluteau, F., Zhang, T. & Han, W. (2022). Reorganization of Asian climate in relation to Tibetan Plateau uplift. Nature Reviews Earth & Environment, 3(10), 684-700. https://doi.org/10.1038/s43017-022-00331-7(Wu et al. 2022)
15. Huber, M., & Goldner, A. (2012). Eocene monsoons. Journal of Asian Earth Sciences, *44*, 3-23. https://doi.org/10.1016/j.jseaes.2011.09.014
16. Licht, A., Van Cappelle, M., Abels, H.A., Ladant, J.B., Trabucho-Alexandre, J., France-Lanord, C., Donnadieu, Y., Vandenberghe, J., Rigaudier, T., Lécuyer, C., Terry Jr., D., Adriaens, R., Boura, A., Guo, Z., Aung Naing, Soe, Quade, J., Dupont-Nivet, G., Jaeger, J.-J., (2014). Asian monsoons in a late Eocene greenhouse world. Nature 513 (7519), 501–506. https://doi.org/10.1038/nature13704

17. Quan, C., Liu, Z., Utescher, T., Jin, J., Shu, J., Li, Y., Liu, Y.S.C. (2014). Revisiting the Paleogene climate pattern of East Asia: a synthetic review. Earth-Sci. Rev.139, 213–230. https://doi .org /10 .1016 /j .earscirev.2014 .09 .005.

18. Farnsworth, A., Lunt, D. J., Robinson, S. A., Valdes, P. J., Roberts, W. H., Clift, P. D., et al. (2019). Past East Asian monsoon evolution controlled by paleogeography, not CO2. Science Advances, 5(10), eaax1697. https://doi.org/10.1126/sciadv.aax1697

19. Spicer, R. A., Yang, J., Herman, A. B., Kodrul, T., Maslova, N., Spicer, T. E., Aleksandrova, G. & Jin, J. (2016). Asian Eocene monsoons as revealed by leaf architectural signatures. Earth and Planetary Science Letters, 449, 61-68. https://doi.org/10.1016/j.epsl.2016.05.036

20. Zhang, Z., Flatøy, F., Wang, H., Bethke, I., Bentsen, M., & Guo, Z. (2012). Early Eocene Asian climate dominated by desert and steppe with limited monsoons. Journal of Asian Earth Sciences, 44, 24-35. https://doi.org/10.1016/j.jseaes.2011.05.013

21. Tardif, D., Toumoulin, A., Fluteau, F., Donnadieu, Y., Le Hir, G., Barbolini, N., Licht, A., Ladant, J.-B., Sepulchre, P., Viovy, N., Hoorn, C. & Dupont-Nivet, G. (2021). Orbital variations as a major driver of climate and biome distribution during the greenhouse to icehouse transition. Science Advances, 7(43), eabh2819. https://doi.org/10.1126/sciadv.abh2819

22. Li, Q., Utescher, T., Liu, Y. C., Ferguson, D., Jia, H., & Quan, C. (2022). Monsoonal climate of East Asia in Eocene times inferred from an analysis of plant functional types. Palaeogeography, Palaeoclimatology, Palaeoecology, 601, 111138. https://doi.org/10.1016/j.palaeo.2022.111138.

23. Meijer, N., Dupont-Nivet, G., Abels, H. A., Kaya, M. Y., Licht, A., Xiao, M., Zhang, Y., Roperch, P., Poujol, M., Lai, Z., & Guo, Z. (2019). Central Asian moisture modulated by proto-Paratethys Sea incursions since the early Eocene. Earth and Planetary Science Letters, 510, 73–84. https://doi.org/10.1016/j.epsl.2018.12.031
24. Stein, R. A., Sheldon, N. D., & Smith, S. Y. (2021). Soil carbon isotope values and paleoprecipitation reconstruction. Paleoceanography and Paleoclimatology, 36(4), e2020PA004158. https://doi.org/10.1029/2020PA004158
25. Breecker, D. O., Sharp, Z. D., & McFadden, L. D. (2009). Seasonal bias in the formation and stable isotopic composition of pedogenic carbonate in modern soils from central New Mexico, USA. The Geological Society of America Bulletin, 121(3–4), 630–640. https://doi.org/10.1130/b26413.1
26. Kelson, J. R., Huntington, K. W., Breecker, D. O., Burgener, L. K., Gallagher, T. M., Hoke, G. D., & Petersen, S. V. (2020). A proxy for all seasons? A synthesis of clumped isotope data from Holocene soil carbonates. Quaternary Science Reviews, 234, 106259. https://doi.org/10.1016/j.quascirev.2020.106259
27. Page, M., Licht, A., Dupont-Nivet, G., Meijer, N., Barbolini, N., Hoorn, C., et al. (2019). Synchronous cooling and decline in monsoonal rainfall in northeastern Tibet during the fall into the Oligocene icehouse. Geology, 47(3), 203–206. https://doi.org/10.1130/g45480.1
28. Licht, A., Kelson, J., Bergel, S., Schauer, A., Petersen, S. V., Capirala, A., Huntington, K. W., Dupont-Nivet, G., Win, Z. & Aung, D. W. (2022). Dynamics of pedogenic carbonate growth in the tropical domain of Myanmar.

Geochemistry, Geophysics, Geosystems, 23(7), e2021GC009929. https://doi.org/10.1029/2021GC009929

29. Licht, A., Dupont-Nivet, G., Meijer, N., Rugenstein, J. C., Schauer, A., Fiebig, J., et al. (2020). Decline of soil respiration in northeastern Tibet through the transition into the Oligocene icehouse. Palaeogeography, Palaeoclimatology, Palaeoecology, 560, 110016. https://doi.org/10.1016/j.palaeo.2020.110016
30. Meijer, N., Dupont-Nivet, G., Licht, A., Roperch, P., Rohrmann, A., Sun, A., Lu, S., Woutersen, A., & Nowaczyk, N. (2023). Early Eocene magnetostratigraphy and tectonic evolution of the Xining Basin, NE Tibet. Basin Research. https://doi.org/10.1111/bre.12720
31. Aminov, J., Dupont-Nivet, G., Ruiz, D., & Gailleton, B. (2023). Paleogeographic reconstructions using QGIS: Introducing Terra Antiqua plugin and its application to 30 and 50 Ma maps. Earth-Science Reviews, 104401. https://doi.org/10.1016/j.earscirev.2023.104401
32. Chen, Z., Ding, Z., Tang, Z., Wang, X., & Yang, S. (2014). Early Eocene carbon isotope excursions: Evidence from the terrestrial coal seam in the Fushun Basin, Northeast China. Geophysical Research Letters, 41(10), 3559-3564. https://doi.org/10.1002/2014GL059808
33. Chen, Z., Wang, X., Hu, J., Yang, S., Zhu, M., Dong, X., Tang, Z., Peng, P. & Ding, Z. (2014). Structure of the carbon isotope excursion in a high-resolution lacustrine Paleocene–Eocene Thermal Maximum record from central China. Earth and Planetary Science Letters, 408, 331-340. https://doi.org/10.1016/j.epsl.2014.10.027
34. Kohn, M. J. (2010). Carbon isotope compositions of terrestrial C3 plants as indicators of (paleo) ecology and (paleo) climate. Proceedings of the National

Academy of Sciences, 107(46), 19691-19695. https://doi.org/10.1073/pnas.100493310

35. Diefendorf, A. F., Mueller, K. E., Wing, S. L., Koch, P. L., & Freeman, K. H. (2010). Global patterns in leaf 13C discrimination and implications for studies of past and future climate. Proceedings of the National Academy of Sciences, 107(13), 5738-5743. https://doi.org/10.1073/pnas.0910513107

36. Chen, Z., Dong, X., Wang, X., Tang, Z., Yang, S., Zhu, M., & Ding, Z. (2020). Spatial change of precipitation in response to the Paleocene-Eocene thermal Maximum warming in China. Global and Planetary Change, 194, 103313. https://doi.org/10.1016/j.gloplacha.2020.103313

37. Beckner, J. R., & Mozley, P. S. (1998). Origin and spatial distribution of early vadose and phreatic calcite cements in the Zia Formation, Albuquerque Basin, New Mexico, USA. Carbonate Cementation in Sandstones: Distribution Patterns and Geochemical Evolution, 27-51. https://doi.org/10.1002/9781444304893.ch2

38. Warren, J. (2000). Dolomite: occurrence, evolution and economically important associations. Earth-Science Reviews, 52(1-3), 1-81. https://doi.org/10.1016/S0012-8252(00)00022-2

39. Eiler, J. M. (2007). “Clumped-isotope” geochemistry—The study of naturally-occurring, multiply-substituted isotopologues. Earth and planetary science letters, 262(3-4), 309-327. https://doi.org/10.1016/j.epsl.2007.08.020

40. Lunt, D. J., Bragg, F., Chan, W. L., Hutchinson, D. K., Ladant, J. B., Morozova, P., Niezgodzki, I., Steinig, S., Zhang, Z., Zhu, J., Abe-Ouchi, A., Anagnostou, E., de Boer, A. M., Coxall, H. K., Donnadieu, Y., Foster, G., Inglis, G. N., Knorr, G., Langebroek, P. M., Lear, C. H., Lohmann, G., Poulsen, C. J., Sepulchre, P.,

Tierney, J. E., Valdes, P. J., Volodin, E. M., Dunkley Jones, T., Hollis, C. J., Huber, M. & Otto-Bliesner, B. L. (2021). DeepMIP: Model intercomparison of early Eocene climatic optimum (EECO) large-scale climate features and comparison with proxy data. Climate of the Past, 17(1), 203-227. https://doi.org/10.5194/cp-17-203-2021

41. Molnar, P. (2022). Differences between soil and air temperatures: Implications for geological reconstructions of past climate. Geosphere, 18(2), 800-824. https://doi.org/10.1130/GES02448.1
42. Hough, B. G., Garzione, C. N., Wang, Z., Lease, R. O., Burbank, D. W., & Yuan, D. (2011). Stable isotope evidence for topographic growth and basin segmentation: Implications for the evolution of the NE Tibetan Plateau. Bulletin, 123(1-2), 168-185. https://doi.org/10.1130/B30090.1
43. Inglis, G. N., Bragg, F., Burls, N. J., Cramwinckel, M. J., Evans, D., Foster, G. L., Huber, M., Lunt, D. J., Siler, N., Steinig, S., Tierney, J. E., Wilkinson, R., Anagnostou, E., de Boer, A. M., Dunkley Jones, T., Edgar, K. M., Hollis, C. J., Hutchinson, D. K. & Pancost, R. D. (2020). Global mean surface temperature and climate sensitivity of the early Eocene Climatic Optimum (EECO), Paleocene–Eocene Thermal Maximum (PETM), and latest Paleocene. Climate of the Past, 16(5), 1953-1968. https://doi.org/10.5194/cp-16-1953-2020
44. Gu, C., & Renaut, R. W. (1994). The effect of Tibetan uplift on the formation and preservation of Tertiary lacustrine source-rocks in eastern China. Journal of Paleolimnology, 11, 31-40. https://doi.org/10.1007/BF00683269
45. Wang, B., Kim, H. J., Kikuchi, K., & Kitoh, A. (2011). Diagnostic metrics for evaluation of annual and diurnal cycles. Climate dynamics, 37, 941-955. https://doi.org/10.1007/s00382-010-0877-0

46. Dupont-Nivet, G., Krijgsman, W., Langereis, C. G., Abels, H. A., Dai, S., & Fang, X. (2007). Tibetan plateau aridification linked to global cooling at the Eocene–Oligocene transition. Nature, *445*(7128), 635-638. https://doi.org/10.1038/nature05516
47. Bowen, G. J., Clyde, W. C., Koch, P. L., Ting, S., Alroy, J., Tsubamoto, T., Wang, Y. & Wang, Y. (2002). Mammalian dispersal at the Paleocene/Eocene boundary. Science, 295(5562), 2062-2065. https://doi.org/10.1126/science.1068700
48. Chaimanee, Y., Chavasseau, O., Beard, K. C., Kyaw, A. A., Soe, A. N., Sein, C., Lazzari, V., Marivaux, L., Marandat, B., Swe, M., Rugbumrung, M., Lwin, T., Valentin, X., Thein, Z. M. M. & Jaeger, J. J. (2012). Late Middle Eocene primate from Myanmar and the initial anthropoid colonization of Africa. Proceedings of the National Academy of Sciences, 109(26), 10293-10297. https://doi.org/10.1073/pnas.1200644109
49. Robin-Champigneul, F., Gravendyck, J., Huasheng, H., Woutersen, A., Pocknall, D., Meijer, N., Dupont-Nivet, G., Erkens, R. H. J., Hoorn, C. (2023) Northward expansion of the southern-temperate podocarp forest during the early Eocene: Palynological evidence from the NE Tibetan Plateau (China). Review of Paleobotany and Palynology, 104914. https://doi.org/10.1016/j.revpalbo.2023.104914
50. Fang, X., Galy, A., Yang, Y., Zhang, W., Ye, C., & Song, C. (2019). Paleogene global cooling–induced temperature feedback on chemical weathering, as recorded in the northern Tibetan Plateau. Geology, 47(10), 992-996. https://doi.org/10.1130/G46422.1

## Methods

### *Sampling*

Rock samples were collected after digging trenches of at least ~0.5 meter deep in the Bingling Shan (BS), Caijia (CJ) and Ledu (LD) sections covering the early to middle Eocene[23,30]. In addition, three horizons with pedogenic carbonate nodules were identified and sampled at the Ledu section. Samples for plant wax analyses were collected using gloves and wrapped in aluminum foil to prevent contamination. Palynological samples were collected from the Bingling Shan and Caijia sections as well as the East Xining (EX), Xiejia (XJ) and Dazhai (DZ) sections[23,30].

### *Composite section and age model*

The individual sections were combined into one composite section using litho- and magnetostratigraphic correlations[30]. First, we assembled the core of the composite section by stitching the Honggou Fm of the Caijia section (CJ) and the Qijiachuan Fm of the Ledu section (LD) together at the liver-brown to red mudrock transition observed in both locations (transition from Qijiachuan to Honggou Fm; blue dashed line Fig. 2 in ref[30]). We assume this to be a chronostratigraphic marker and define it as the 0 meter-level in the composite log. The stratigraphic positions of these sections can be converted to the composite stratigraphic position as follows:

Comp m level = CJ [44.5m to 280m] - 44.5
Comp m level = LD [entire section] - 15

Next, we project the Qijiachuan Fm of the Caijia (CJ) and Bingling Shan (BS) sections on the composite section making sure that the lithostratigraphic boundaries between the evaporites of the middle Qijiachuan Fm and the liver-colored mudrocks of the upper Qijiachuan Fm correlate. This is necessary because the thicknesses of the formations vary between the sections and the transition between these formations is assumed to represent a chronostratigraphic marker. The stratigraphic positions of these sections can be converted to the composite stratigraphic position as follows:

Caijia:
Comp m level = (CJ[2m to 44.5m] - 44.5) * (1 - 5.9 / 42.5)
= CJ[0 to 2m] - 38.6
Bingling Shan:
Comp m level = ((BS[5.2m to 43m] - 79.6) + ((BS[5.2m to 43m] - 43) / -37.8) * 8.05)
= BS[43m and higher] - 79.6

Based on our observation of the large negative CIE, we propose to revise the age model of ref[30]. The previous age model is reliable down to chron C22n and constrained by the radiometric age of a tuff[23]. However, chron C23n below is very short and does not fit the pattern of the geomagnetic polarity timescale[30]. Hence, we infer an unconformity at the base of C23n which also corresponds to the lithological shift from calcareous to dolomitic mudrocks (Fig. 2). The negative CIE occurs within a long reversed polarity zone on top of a short normal zone. This polarity pattern fits well with C25n and C24r and is within the radiometric age constraints of 53.7±3.3 Ma recorded in a carbonate bed just below the CIE (Fig. 2)[30]. The PETM and ETM2 occur in C24r and could correlate with the CIE in the Xining Basin as discussed in the main text. Throughout the manuscript we use the geomagnetic polarity timescale of ref[4] for correlating our paleo-environmental data with the Cenozoic Global Reference benthic foraminifera carbon and oxygen Isotope Dataset (CENOGRID).

### *XRD*

X-ray diffractometry (XRD) analyses were performed on 27 mudrock samples and 5 carbonate beds throughout the stratigraphy to assess the mineralogy and the carbonate type. Powdered rock samples were measured using a PANALYTICAL X'Pert Bragg-Brentano diffractometer using a copper beam powered by 30 mA and 40 KV generator current. The characteristic diffraction maxima of the mineral phases were determined using the MacDiff software (http://mill2.chem.ucl.ac.uk/ccp/web-mirrors/krumm/html/software/macdiff.html). Intensities were converted to 1° divergence characteristics and weighted by reference intensity ratios (RIR) to semiquantitatively calculate the relative abundance of each mineral phase. The identified mineral phases are (Extended Data Fig. 3): mixed-layer illite-smectite (main diffraction maxima position: 10.4 Å, RIR value: 0.52), illite/muscovite (10.0 Å, 0.43), chlorite (14.0 Å, 1.00), analcime (3.43 Å, 1.41), quartz (4.26 Å and 3.34 Å, 3.03) K-feldspar (3.25 Å, 0.60), albite (3.20 Å, 0.64), calcite (3.04 Å, 2.20) and calcian dolomite (2.91 Å, 2.51). The mol% of $MgCO_3$ in the calcian dolomite was estimated using the relative position of the 104 peak (d in Å) compared to calcite (3.035 Å) and stoichiometric dolomite (2.885 Å):

$$Mol\%\ MgCO_3 = \frac{3.035 - d}{3.035 - 2.885} \times 50\%$$

*Compound-specific lipid biomarkers and stable isotopes*

Plant waxes were extracted from 25 mudrock and gypsiferous mudrock samples at the Organic Surface Geochemistry Lab (OSGLab) at the German Research Centre for Geosciences (GFZ) in Potsdam. Samples were crushed and then powdered using a shatterbox with an agate grinding chamber. Soluble organic matter was extracted using a Dionex accelerated solvent extractor (ASE 350) with a dichloromethane/methanol mixture of 9:1 at 100°C and 1500 psi. Total extracts of three 18-minute cycles were captured in 250 ml bottles, later concentrated to 4 ml in a Turbovap, and then separated on silica gel using a solid phase extraction (SPE) as described in ref[51]. The $C_{27}$, $C_{28}$, $C_{29}$, $C_{30}$, $C_{31}$, $C_{32}$, and $C_{33}$ *n*-alkanes were identified and quantified using a gas chromatograph with a coupled flame ionization and mass-selective detector (GC-FID/MSD Agilent 7890A GC, 5975C MSD) flushed with helium carrier gas. Temperatures in the GC oven were programmed to increase at a rate of 12°C/min starting from 70°C to 320°C at which temperatures were held constant for 21 min. The PTV injector had a split ratio of 5:1 at an initial temperature of 70°C. The n-alkane FID-peak areas were compared with a previously added 5$\alpha$-androstane standard from which n-alkane concentrations were calculated. The n-alkane concentrations are reported as µg/gram dry sediment. In addition the average chain-length (ACL) and the carbon preference index (CPI) were calculated.

For all samples compound specific stable isotope values were measured using a GC-Isolink coupled to a Thermo Scientific MAT 253 isotope ratio mass spectrometer (IRMS) at the Stable Isotope and Organic Molecular Biogeochemistry Laboratory at the University of Connecticut. The *n*-alkane fractions were dried and concentrated to 200 µg/µl per compound in hexane for $\delta^2H_{wax}$ measurements. Each sample was measured in at least duplicate and in most samples triplicate analysis. The injector of the GC was operated in splitless mode at 300°C and the oven was held at 70°C for 2 minutes. The oven was heated at 15°C/min until 150°C, then heated with 5°C/min to 320°C. The final temperature was held for 10 minutes. The column effluent was transferred into an isotope ratio mass spectrometer after conversion to $H_2$ in a high-temperature oven at 1420°C. Stable isotopes are reported in delta notation in permil (‰). The standard deviation for each sample was better than 3‰ and the $\delta^2H_{wax}$ are reported in Vienna Standard Mean Ocean Water scale (VSMOW). $\delta^{13}C_{wax}$ values were measured using the same fractions used for $\delta^2H_{wax}$. The *n*-alkane fractions were concentrated to 60 µg/µl in hexane for $\delta^{13}C_{wax}$ measurements. The same instrumental setup (GC-IRMS) and temperature programming was used as for the $\delta^2H_{wax}$ measurements, only the oxidation oven was run at a lower temperature of 960°C. Duplicates were measured for each sample and a $CO_2$ gas with known isotopic composition was used as reference gas and $\delta^{13}C_{wax}$ values are reported in Vienna Pee Dee Belemnite scale (VPDB). The analytical precision of each sample had a typical standard deviation of 0.5‰. Isotopic compositions were standardized using a suite of *n*-alkanes in a standard mixture.

### *Stable and clumped isotopes*

Bulk organic stable isotopes were measured on 113 mudrock and gypsiferous mudrock samples. These samples were decarbonated twice with 6N HCl and washed with 18 M-Ohm water several times for acid removal; carbon content and organic matter $\delta^{13}C$ values were then measured. Samples from the Ledu section were measured using a Costech ECS 4010 Elemental Analyzer coupled to a Thermo

Scientific MAT 253 gas source IRMS at the University of Washington. Samples from the Caijia section were measured using a Flash Elemental Analyzer 1112 connected to a Thermo Scientific MAT 253 IRMS at the Goethe University-Senckenberg BiK-F Stable Isotope Facility in Frankfurt. Samples from the Bingling Shan section were measured using a Flash Elemental Analyzer 2000 coupled to a Thermo Scientific Delta-V IRMS at the Alfred-Wegener Institute Isotope Laboratory (AWI) in Potsdam. Measured $\delta^{13}C$ values (all relative to VPDB) were corrected using in-house reference materials and long-term repeatability was below 0.2‰. International reference materials USGS 24 and IAEA-CH-7 were analyzed along with the samples to check for accuracy.

Carbonate stable isotopes were measured on 51 calcite-bearing mudrocks and 3 pedogenic carbonate nodules. The calcite-bearing mudrocks were reacted with 105 % orthophosphoric acid and carbonate $\delta^{18}O$ and $\delta^{13}C$ values were then measured. Samples from the Ledu section were measured using a Thermo Scientific Kiel III Carbonate Device coupled to a Thermo Scientific Delta Plus IRMS at University of Washington. Samples from the Caijia section were measured with a Thermo Scientific GasBench II interfaced with a Thermo Scientific MAT 253 IRMS at the Goethe University-Senckenberg BiK-F Stable Isotope Facility. Measured carbon and oxygen isotopic compositions were corrected using in-house reference materials as well as NBS18 and NBS19 carbonate reference materials. Long-term repeatability was below 0.03‰ for $\delta^{13}C$ and below 0.06‰ for $\delta^{18}O$. All $\delta^{13}C$ and $\delta^{18}O$ values are expressed relative to VPDB.

Clumped isotopes were analyzed on 16 of these calcite-bearing mudrocks and on the 3 pedogenic nodules at the Goethe University-Senckenberg BiK-F Stable Isotope Facility, using a Thermo Scientific Kiel IV Carbonate Device paired with a Thermo Scientific MAT 253 Plus IRMS. The Kiel IV was modified from its original configuration with the addition of two water traps and a different heating-cooling system on the purification trap. Depending on the carbonate content, 110 to 2500 µg of sample was reacted with 105% orthophosphoric acid at 70°C for 5 minutes starting from the last acid drop. In each sequence, half of the analyses were reserved for measurement of the ETH carbonate standards[52], with ETH 1 and 2 measured in equal numbers as ETH 3, and with ETH 4 less frequently. Data were corrected for negative background using intensities measured on the 47.5 Faraday cup during acquisition, scaled by a factor that minimizes the slope between ETH 1 and 2. Baseline corrected data were projected into the Intercarb Carbon-Dioxide Equilibrium Scale (I-CDES)[52] using the "independent" approach in the python package D47crunch[53]. The resulting $\Delta_{47}$ values were converted into temperature using the calibration of ref[54]. Each sample was measured in 13 to 18 replicates and the errors are reported as both 68% and 95% confidence intervals (1SE and 2SE respectively). Long-term repeatability of both samples and ETH standards was 0.035‰.

The $\delta^{18}O$ values of the soil water ($\delta^{18}O_{water}$) are reconstructed using the $\Delta_{47}$-derived temperatures and the equation of ref[55]. These values are compared with modern-day $\delta^{18}O_{water}$ values of the summer monsoon and wintertime westerlies[56] (Extended Data Fig. 5).

*Palynology*

The palynological samples were prepared by Palynological Laboratory Services (Anglesey, UK) using standard palynological techniques (HCL, HF, sieving at 10µm), the University of Amsterdam (Amsterdam, the Netherlands; HCL, sieving at 212µm, 20% pyrophosphate, acetolysis, bromoform treatment), and at the Sediment Laboratory of the Vrije Universiteit (Amsterdam, the Netherlands; following methods of ref[57] and described in ref[58]). Plant Functional Types (PFTs) were assigned using the Nearest Living Relatives (NLR) approach applied by ref[59].

*MAP reconstruction*

We use an empirical relationship which can be used to reconstruct Mean Annual Precipitation (MAP) using the $\delta^{13}C_{SOM}$ values of top soils (O- and A-horizons)[24]. The organic matter in deeper horizons might be affected by decomposition resulting in fractionation to higher $\delta^{13}C_{SOM}$ values[60], which would lead to an underestimation of the MAP. The alluvial mudflat deposits of the Xining Basin show clear evidence of pedogenesis such as vertic slickensides, mudcracks, mottling, blocky peds, and clay coatings in thin sections, but no obvious horizonation due to overprinting of stacked paleosols. It is therefore impossible to preselect only O- and A-horizons. Nevertheless we argue that the bulk $\delta^{13}C_{SOM}$ values and the CIE are not strongly affected by degradation because we observe no clear relationship between $\delta^{13}C_{SOM}$ and total organic content (Extended Data Fig. 2) and the $\delta^{13}C_{SOM}$ values of alluvial mudflats are indistinguishable from laterally equivalent gypsum beds which have a high quality of organic preservation[59]. In addition, an even larger CIE is observed in the *n*-alkanes

($\delta^{13}C_{wax}$) which are less affected by degradation[61]. If this difference in CIE is caused by the decomposition of bulk organic matter, the actual CIE and precipitation changes could be even larger and our MAP reconstructions should be considered as a minimum estimate.

Before using the paleoprecipitation proxy, we correct the $\delta^{13}C_{SOM}$ values to account for the different $CO_2$ $\delta^{13}C$ values ($\delta^{13}C_{atm}$) of the Paleocene/Eocene atmosphere compared to the pre-industrial value of -6.5‰ that is implicit in the empirical relation[24]. We apply a -1.5‰ correction to the $\delta^{13}C_{SOM}$ values to correct for the baseline Paleocene ($\delta^{13}C_{atm}$ = -5.0‰)[62], a +3.1‰ correction for the PETM assuming a lowering of 4.6‰ ($\delta^{13}C_{atm}$ = -9.6‰) through the injection of $^{13}C$-depleted carbon[35,62] and a -1.0‰ correction for the early Eocene baseline ($\delta^{13}C_{atm}$ = -5.5‰)[62]. Other early Eocene hyperthermals corresponded to smaller isotope excursions than the PETM and we use a lowering of 3.0‰ ($\delta^{13}C_{atm}$ = -8.5‰) to illustrate the effect on the MAP reconstruction. The MAP is then calculated using the following equation[24]:

$$\text{MAP (mm/year)} = \exp\left( (\delta^{13}C_{SOM} + 11.94) / -2.04\right)$$

### *Carbonate characterization*

We have characterized the carbonates of the Xining strata following the methods of ref[27]. Thin sections were prepared for six representative mudrock samples and three carbonate nodules. These were examined using cathodoluminescence (CL) and plane- and cross-polarized microscopy to examine the origin and possible diagenesis of the carbonates. The samples were examined at the University of Potsdam using an Olympus BXFM-F polarizing microscope equipped with a lumic hot-cathode electron source and an Olympus XC10 digital color camera. In addition, seven powdered samples were mounted on a stub and carbon coated. These were further examined at the University of Potsdam using a JEOL JSM-6510 Scanning Electron Microscope (SEM) coupled to an Oxford Instruments INCAx-act Energy Dispersive X-ray Spectrometer (EDS) to assess their mineralogy.

The calcite is a dull luminescent micrite and is observed throughout the clayey matrix (Extended Data Fig. 4 A, B). Some brighter specks of microspar are observed as well but no detrital carbonate grains nor blocky sparite in cracks, veins or vugs which would have been typical for phreatic cements[37,63]. These observations are very similar to ref[27] and we follow their interpretation of an early diagenetic cement forming in the vadose zone from either shallow groundwater or percolating soil water[37,63]. The $\delta^{18}O_{carb}$ values are consistent with coeval pedogenic carbonates in the region[10] and the $\delta^{13}C_{carb}$ are very low (~-9‰ in Caijia and ~-11‰ in Ledu) as is expected during the negative CIE (Extended Data Fig. 5). The stable isotope values do show some positive linear relation (Extended Data Fig. 6) indicating the effects of evaporation[64]. This suggests that the carbonates formed relatively close to the surface of the paleosol. The calcite occurs in a specific stratigraphic interval in multiple locations of the basin (Fig. 2), which suggests a primary origin rather than precipitation/reprecipitation during modern-day weathering which would have affected all mudrocks. In addition, Eocene climatic events such as the EOT have been recorded in these calcite cements with no indication for overprinting[27].

In addition to the calcareous mudrocks, three horizons with pedogenic nodules were observed in the Ledu section. Most of these nodules are entirely composed of micrite and floating detrital grains (Extended Data Fig. 4 C), but some contain vugs filled with sparite indicating a phreatic overprint. These were carefully avoided when powdering the samples for isotopic analyses. The nodules occurring in the coarse sandstone (at 53.3 Ma) show features of a mixed origin. The floating grains show an isopachous rim of microspar / sparite while the rest of the matrix is filled with micrite (Extended Data Fig. S4 D). This indicates an initial vadose origin for the micrite which is overprinted by phreatic cements filling circum-granular cracks[37].

Dolomite occurs as rhombic crystals within the mudrock matrix (Extended Data Fig. 4 E and F), but also as massive cm-scale beds interbedding lacustrine mudrocks (Extended Data Fig. 4 G) and as cm-scale burrows (Extended Data Fig. 4 H). The SEM-EDS analysis revealed that the dolomites are non-ferroan but calcian dolomite with an XRD peak at ~2.91 Å (Extended Data Fig. 3) and $MgCO_3$ contents ranging from 44 to 46%. No dolomite has been reported from the mountain ranges surrounding the Xining Basin[65] and a detrital origin is therefore unlikely. Instead, the dolomite could have formed either by diagenetic replacement of calcite or syn-sedimentary / early-diagenetic precipitation from saline brines on a mudflat [38,66-68]. We note that the dolomite co-occurs in a specific stratigraphic interval with analcime, which typically forms in saline brines[69], and with increased concentrations of hematite[70] indicative of dry conditions[71]. This suggests a paleo-environmental control on the formation of calcian dolomite, but we cannot rule out the role of diagenetic replacement.

*DeepMIP climate model simulations*

We use the DeepMIP climate model ensemble[40] to compare our proxy reconstructions with simulated early Eocene precipitation and temperature estimates. The paleolocation of the Xining Basin was reconstructed using the hotspot reference frame ref[72] at 55 Ma (https://www.odsn.de/odsn/services/paleomap/paleomap.html). This resulted in a paleolocation (102.5°N, 39.5°E) which fits well in relation to paleotopographic features such as the Hangay Dome and Qinling belt that are observed on the paleogeographic map used in the DeepMIP simulations[73].

## Data availability

Palynology counts, TOC and bulk organic $\delta^{13}C$, *n*-alkane $\delta^{13}C$ and $\delta^{2}H$, XRD bulk mineralogy and carbonate $\delta^{13}C$, $\delta^{18}O$ and $\Delta_{47}$ are available at https://doi.org/10.1594/PANGAEA.962894. The DeepMIP preindustrial and Eocene climate model simulations are available by following the instructions at https://www.deepmip.org/data-eocene/. The weather station data from Xining and Tashkent is available at https://www.ncei.noaa.gov/products/wmo-climate-normals.

## Methods references

51. Rohrmann, A., Sachse, D., Mulch, A., Pingel, H., Tofelde, S., Alonso, R. N., & Strecker, M. R. (2016). Miocene orographic uplift forces rapid hydrological change in the southern central Andes. Scientific reports, 6(1), 35678. https://doi.org/10.1038/srep35678
52. Bernasconi, S., Daëron, M., Bergmann, K., Bonifacie, M., Meckler, A. N., Affek, H., et al. (2021). InterCarb: A community effort to improve inter-laboratory standardization of the carbonate clumped isotope thermometer using carbonate standards.

53. Daëron, M. (2021). Full propagation of analytical uncertainties in Δ47 measurements. Geochemistry, Geophysics, Geosystems, 22(5), e2020GC009592. https://doi.org/10.1029/2020GC009592

54. Anderson, N. T., Kelson, J. R., Kele, S., Daëron, M., Bonifacie, M., Horita, J., et al. (2021). A unified clumped isotope thermometer calibration (0.5–1100°C) using carbonate-based standardization. Geophysical Research Letters, 48(7), e2020GL092069. https://doi.org/10.1029/2020gl092069

55. Kim, S. T., & O'Neil, J. R. (1997). Equilibrium and nonequilibrium oxygen isotope effects in synthetic carbonates. Geochimica et cosmochimica acta, 61(16), 3461-3475. https://doi.org/10.1016/S0016-7037(97)00169-5

56. Araguás-Araguás, L., Froehlich, K., & Rozanski, K. (1998). Stable isotope composition of precipitation over Southeast Asia. Journal of Geophysical Research, 103(D22), 28721–28742. https://doi.org/10.1029/98jd02582

57. Horowitz, A. (1992). Palynology of arid lands. Elsevier Science, 568 p.

58. Dupont-Nivet, G., Hoorn, C., & Konert, M. (2008). Tibetan uplift prior to the Eocene-Oligocene climate transition: Evidence from pollen analysis of the Xining Basin. Geology, 36(12), 987–990. https://doi.org/10.1130/G25063A.1

59. Hoorn, C., Straathof, J., Abels, H. A., Xu, Y., Utescher, T., & Dupont-Nivet, G. (2012). A late Eocene palynological record of climate change and Tibetan plateau uplift (Xining Basin, China). Palaeogeography, Palaeoclimatology, Palaeoecology, 344, 16–38. https://doi.org/10.1016/j.palaeo.2012.05.011

60. Wynn, J. G. (2007). Carbon isotope fractionation during decomposition of organic matter in soils and paleosols: implications for paleoecological interpretations of paleosols. Palaeogeography, Palaeoclimatology,

Palaeoecology, 251(3-4), 437-448. https://doi.org/10.1016/j.palaeo.2007.04.009

61. Diefendorf, A. F., & Freimuth, E. J. (2017). Extracting the most from terrestrial plant-derived n-alkyl lipids and their carbon isotopes from the sedimentary record: A review. Organic Geochemistry, 103, 1-21. https://doi.org/10.1016/j.orggeochem.2016.10.016
62. Tipple, B. J., Meyers, S. R., & Pagani, M. (2010). Carbon isotope ratio of Cenozoic CO2: A comparative evaluation of available geochemical proxies. Paleoceanography, 25(3). https://doi.org/10.1029/2009PA001851
63. Mack, G. H., Cole, D. R., & Treviño, L. (2000). The distribution and discrimination of shallow, authigenic carbonate in the Pliocene–Pleistocene Palomas Basin, southern Rio Grande rift. Geological Society of America Bulletin, 112(5), 643-656. https://doi.org/10.1130/0016-7606(2000)112<643:TDADOS>2.0.CO;2
64. Quade, J., Rech, J. A., Latorre, C., Betancourt, J. L., Gleeson, E., & Kalin, M. T. (2007). Soils at the hyperarid margin: the isotopic composition of soil carbonate from the Atacama Desert, Northern Chile. Geochimica et Cosmochimica Acta, 71(15), 3772-3795. https://doi.org/10.1016/j.gca.2007.02.016
65. Bureau of Geological and Mineral Resources of Qinghai Province (BGMRQP). (1965). Regional geological survey reports of Ledu sheet (1:200000), Qinghai Province, P.R. China (in Chinese).
66. Last, W. M. (1990). Lacustrine dolomite—an overview of modern, Holocene, and Pleistocene occurrences. Earth-Science Reviews, 27(3), 221-263. https://doi.org/10.1016/0012-8252(90)90004-F

67. Peterson, M. N. A., Bien, G. S., & Berner, R. A. (1963). Radiocarbon studies of recent dolomite from Deep Spring Lake, California. Journal of Geophysical Research, 68(24), 6493-6505. https://doi.org/10.1029/JZ068i024p06493

68. Wolfbauer, C. A., & Surdam, R. C. (1974). Origin of nonmarine dolomite in Eocene Lake Gosiute, Green River Basin, Wyoming. Geological Society of America Bulletin, 85(11), 1733-1740. https://doi.org/10.1130/0016-7606(1974)85<1733:OONDIE>2.0.CO;2

69. Remy, R. R., & Ferrell, R. E. (1989). Distribution and origin of analcime in marginal lacustrine mudstones of the Green River Formation, south-central Uinta Basin, Utah. Clays and Clay minerals, 37, 419-432. https://doi.org/10.1346/CCMN.1989.0370505

70. Fang, X., Zan, J., Appel, E., Lu, Y., Song, C., Dai, S., & Tuo, S. (2015). An Eocene–Miocene continuous rock magnetic record from the sediments in the Xining Basin, NW China: Indication for Cenozoic persistent drying driven by global cooling and Tibetan Plateau uplift. Geophysical Journal International, 201(1), 78–89. https://doi.org/10.1093/gji/ggv002

71. Lepre, C. J., & Olsen, P. E. (2021). Hematite reconstruction of Late Triassic hydroclimate over the Colorado Plateau. Proceedings of the National Academy of Sciences, 118(7), e2004343118. https://doi.org/10.1073/pnas.2004343118

72. Müller, R. D., Royer, J. Y., & Lawver, L. A. (1993). Revised plate motions relative to the hotspots from combined Atlantic and Indian Ocean hotspot tracks. Geology, 21(3), 275-278. https://doi.org/10.1130/0091-7613(1993)021<0275:RPMRTT>2.3.CO;2

73. Herold, N., Buzan, J., Seton, M., Goldner, A., Green, J. A. M., Müller, R. D., Markwick, P. & Huber, M. (2014). A suite of early Eocene (~ 55 Ma) climate

model boundary conditions. Geoscientific Model Development, 7(5), 2077-2090. https://doi.org/10.5194/gmd-7-2077-2014

74. Laskar, J., Fienga, A., Gastineau, M., & Manche, H. (2011). La2010: a new orbital solution for the long-term motion of the Earth. Astronomy & Astrophysics, 532, A89. https://doi.org/10.1051/0004-6361/201116836

## Extended Data

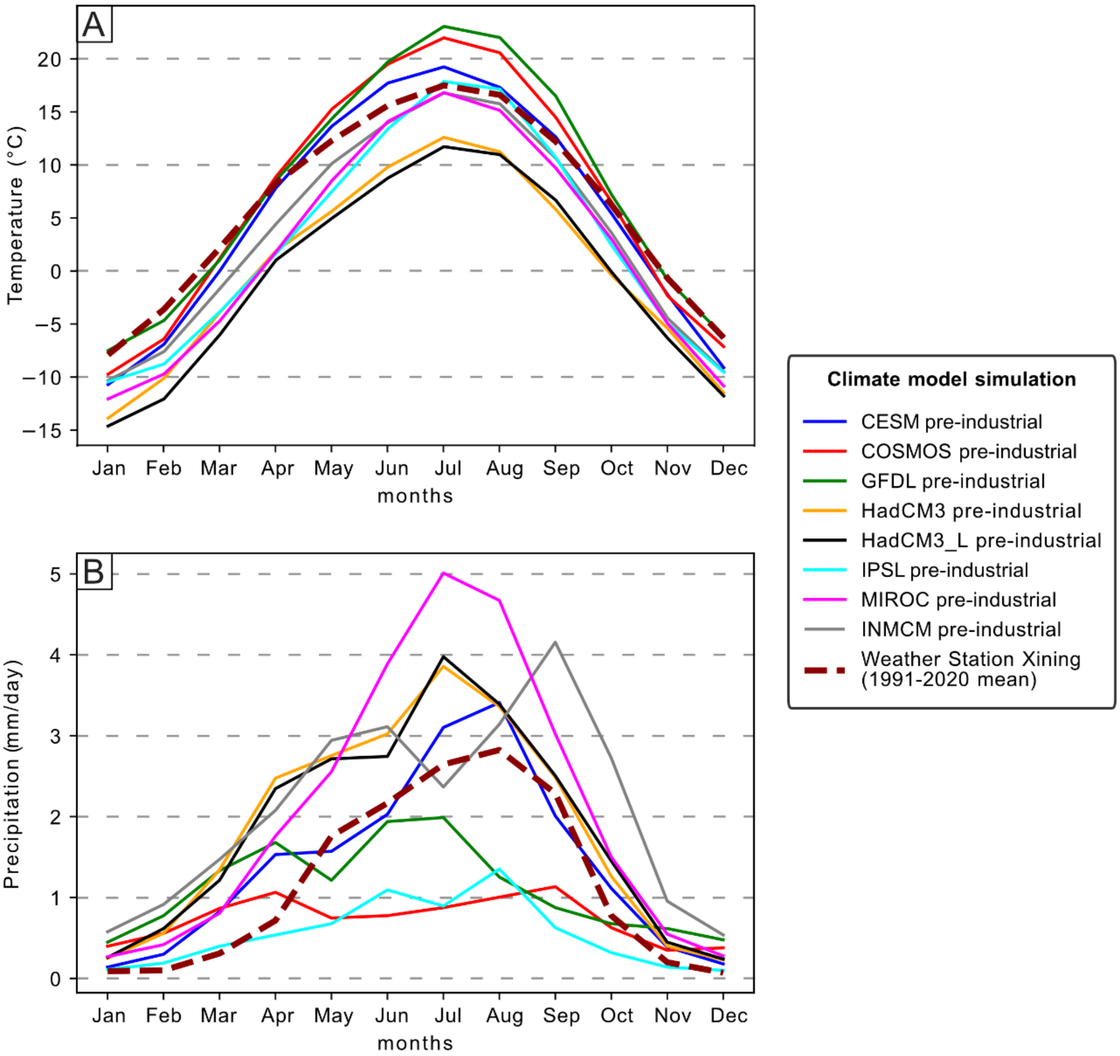

*Extended Data Fig. 1. Pre-industrial control simulations and weather station data from the Xining Basin. Weather station precipitation data (https://www.ncei.noaa.gov/products/wmo-climate-normals) and pre-industrial control*

962 *simulations of A) temperature and B) precipitation in the Xining Basin using the*
963 *DeepMIP climate model ensemble.*

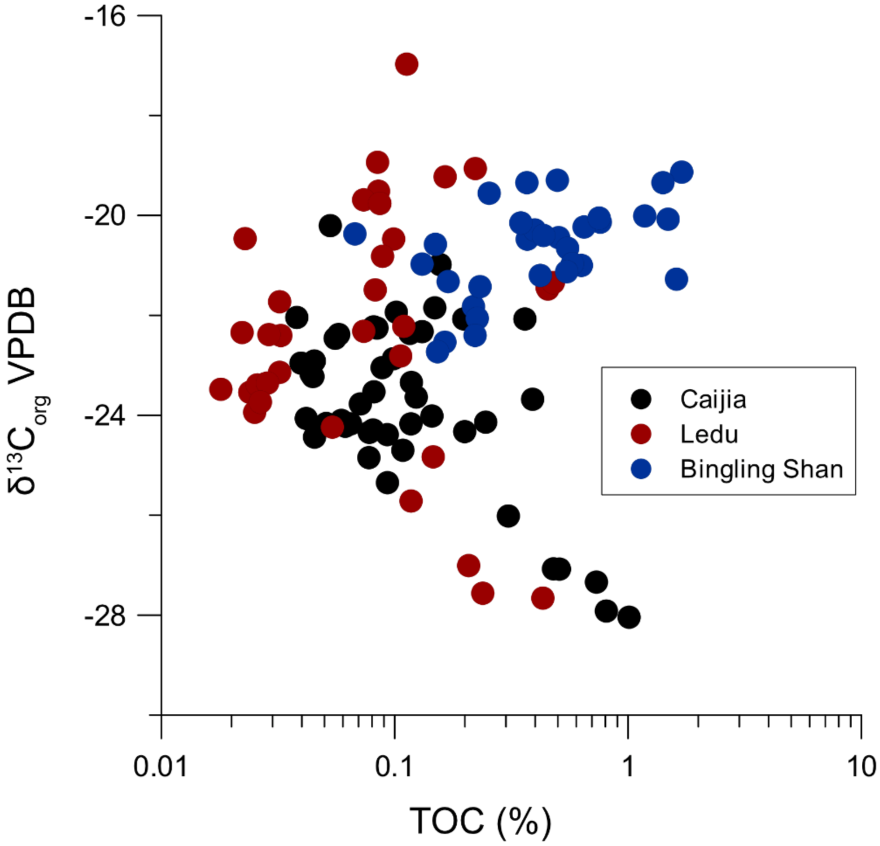

964

965 *Extended Data Fig. 2. Soil organic matter δ$^{13}$C versus Total Organic Content (TOC).*

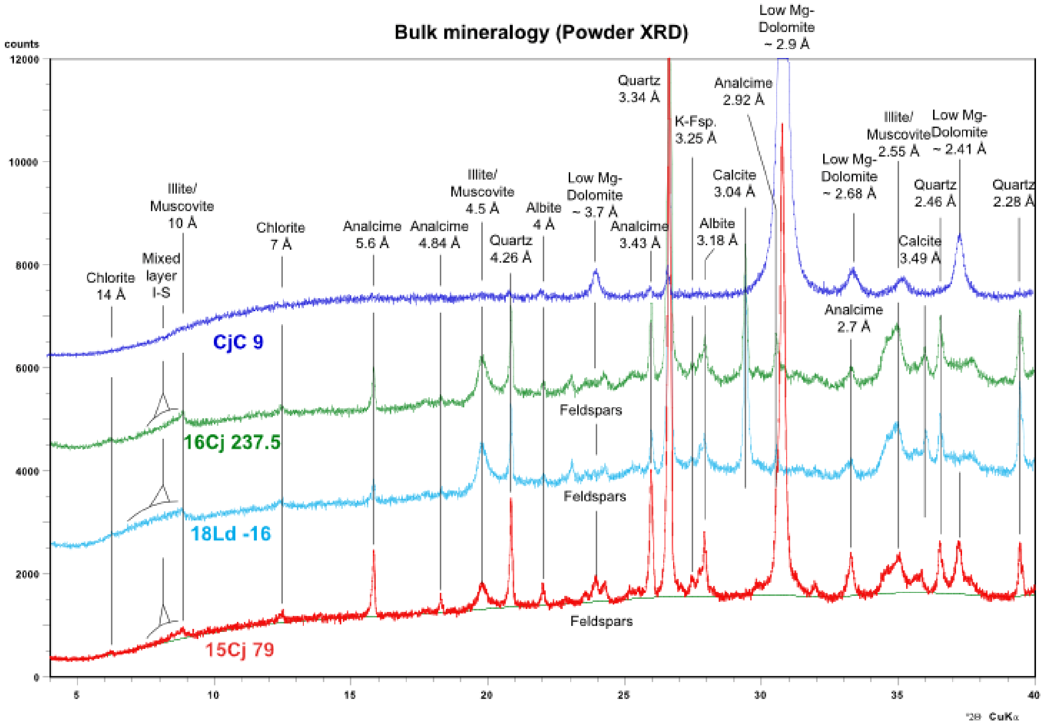

*Extended Data Fig. 3. XRD diffractograms showing the dominant peaks and bulk mineralogy of selected samples including: a dolomite bed (CjC9, as shown on Extended Data Fig. 4G; composite position: -37.1 m), a calcareous mudrock (16Cj237.5; composite position: 193 m), a calcareous mudrock from the CIE interval (18Ld-16; composite position: -31m) and a dolomitic mudrock (15Cj79; composite position: 54 m). The samples 16Cj237.5 and 18Ld-16 were used for stable and clumped isotope analyses.*

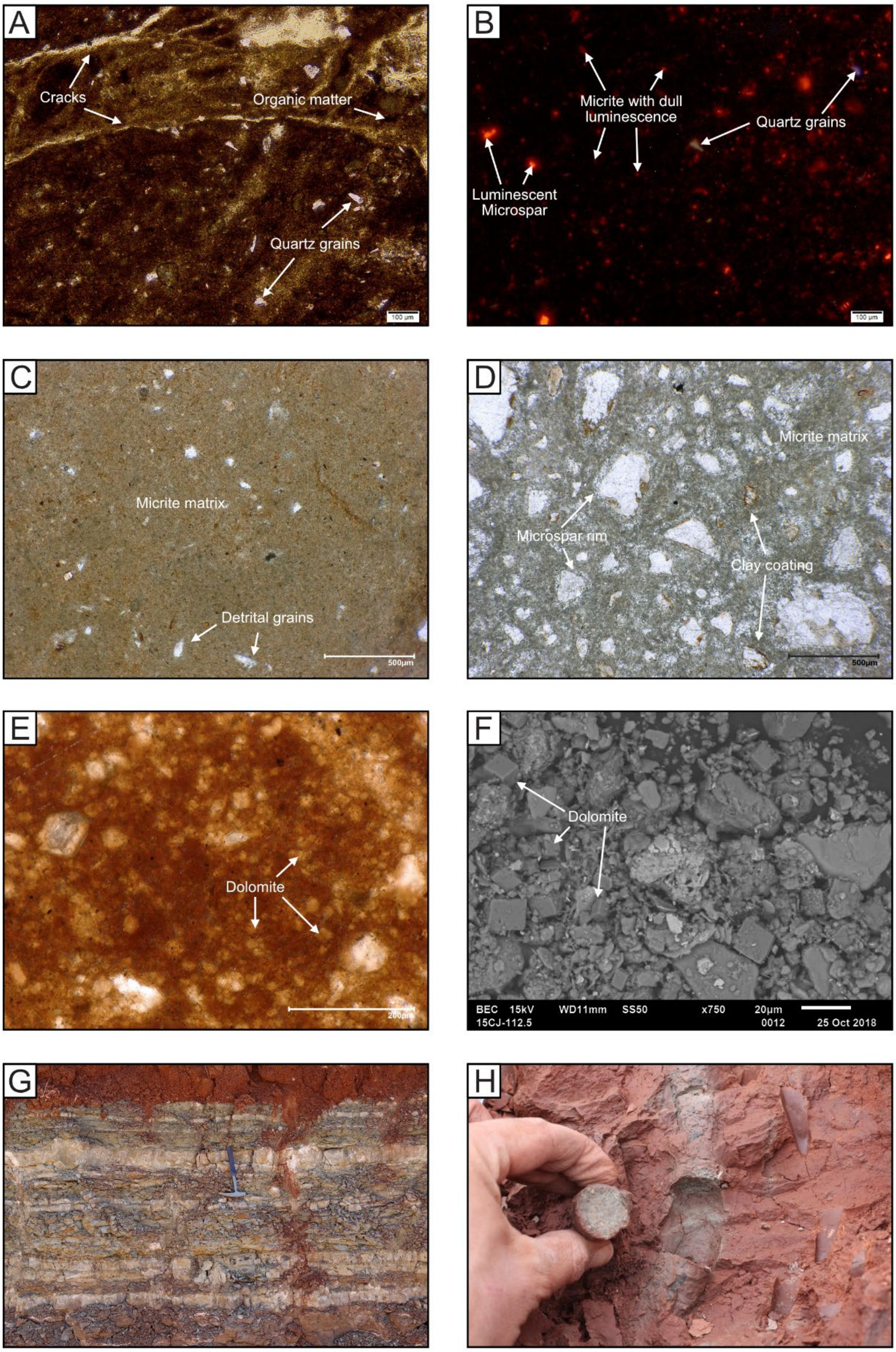

*Extended Data Fig. 4. Microscope and field photographs. A) and B) Cross-polarized and cathodoluminescence image of a mudrock sample with vadose-grown calcite cement (18LD-15; Ledu section; -15 meter-level) showing silt-sized matrix with* *dispersed organic matter, dull luminescent micrite and some luminescent microsparite and sparite. Plane-polarized images of pedogenic nodules showing: C) Micrite matrix with floating detrital grains in 18LD+4nodB (Ledu section; 12.3 meter-level). D) Floating detrital grains with isopachous microsparite to sparite rim and micritic matrix in 18LDconglonod (Ledu section; -60 meter-level). Massive red dolomitic mudrock samples showing rhombohedral dolomite crystals in E) plane-polarized light (15CJ-111_75; Caijia section 131.25 meter-level) and F) SEM (15CJ-112_5; Caijia section; 132 meter-level). G) Greenish lacustrine mudrocks interbedded with massive dolomite beds (Caijia section; 75 meter-level), hammer for scale. H) Dolomite-filled burrow (Caijia section; 93 meter-level).*

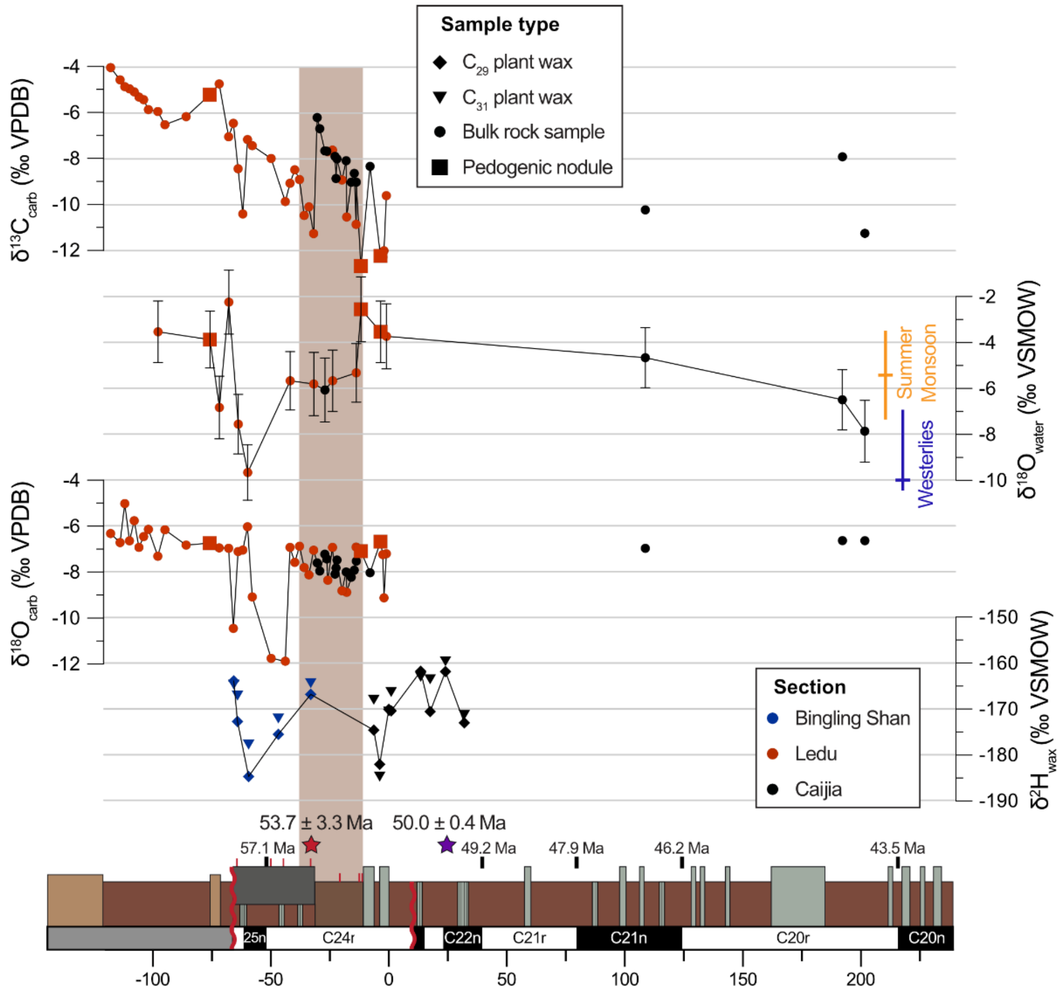

*Extended Data Fig. 5. Carbonate and plant wax stable isotopes. Stable isotope record ($\delta^{18}O_{carb}$ and $\delta^{13}C_{carb}$) of the vadose-grown and pedogenic carbonates and $\delta^{2}H_{wax}$ values of plant waxes. $\delta^{18}O$ values of the soil water ($\delta18O_{water}$) are reconstructed using the $\Delta_{47}$-derived temperatures. Modern-day $\delta^{18}O_{water}$ values of the summer monsoon and wintertime westerlies are shown[57].*

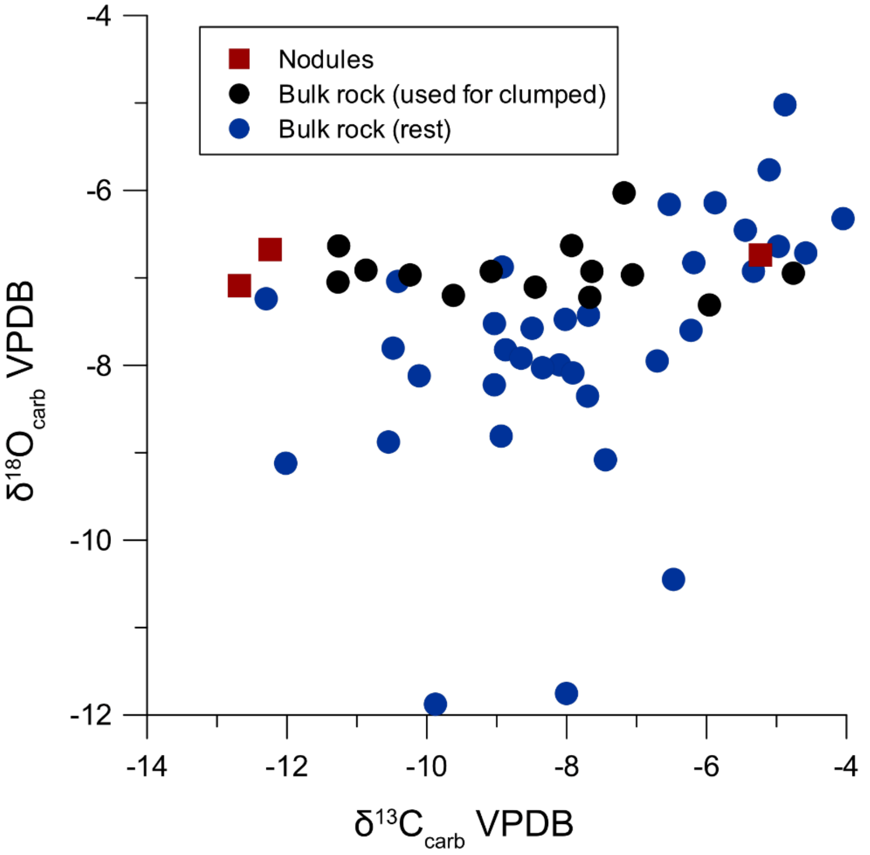

*Extended Data Fig. 6. Carbonate stable isotope biplot. Stable isotope biplot of the studied calcites.*

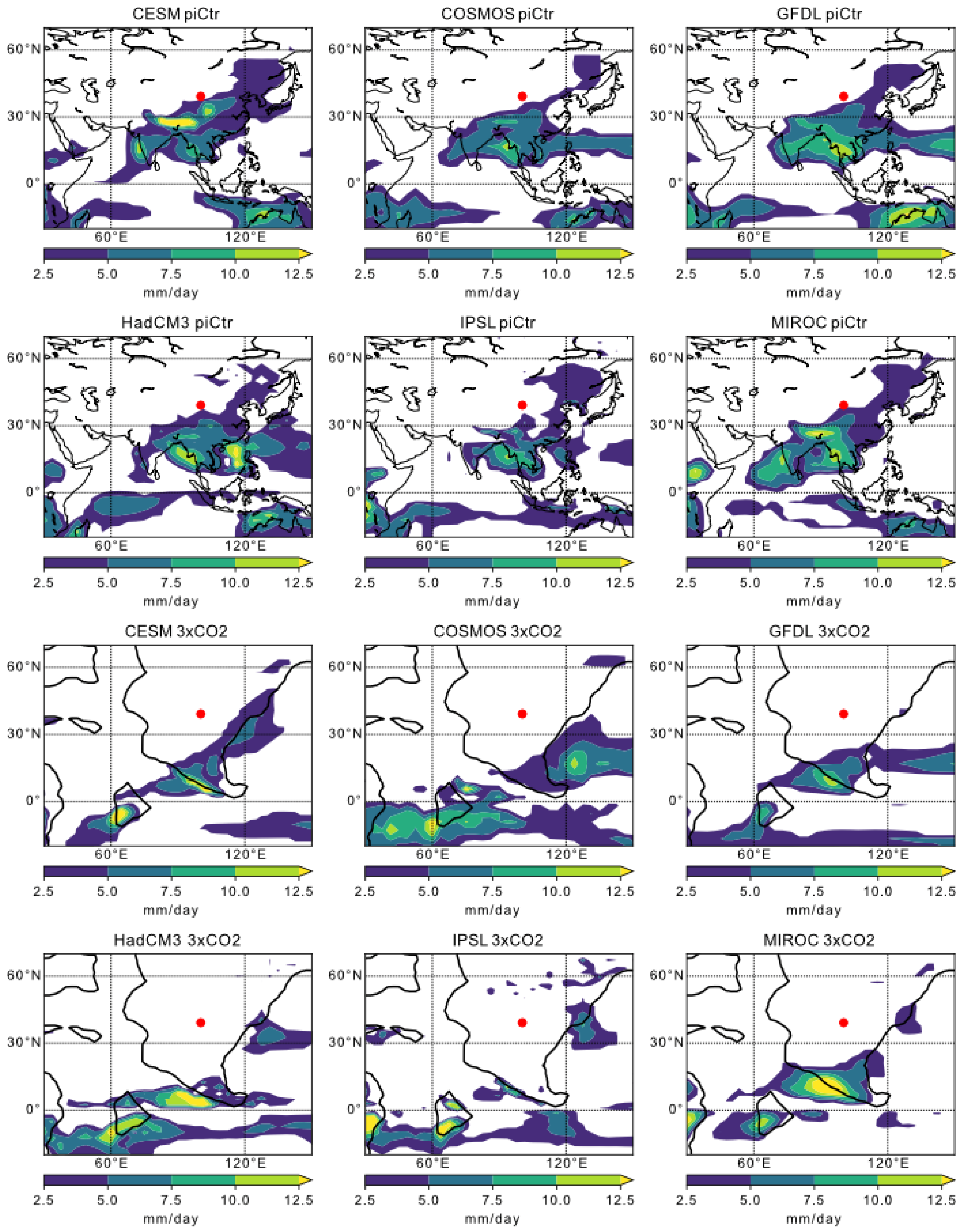

*Extended Data Fig. 7. Monsoonal domains in DeepMIP climate model simulations. Distribution of monsoonal domains in the pre-industrial control and 3x pCO*$_2$ *Eocene DeepMIP simulations. Summer (MJJAS) minus winter precipitation (NDJFM) is used* *as a metric and regions where this difference is > 2.5 mm/day are considered monsoonal[44]. Red dot indicates the location of the Xining Basin.*

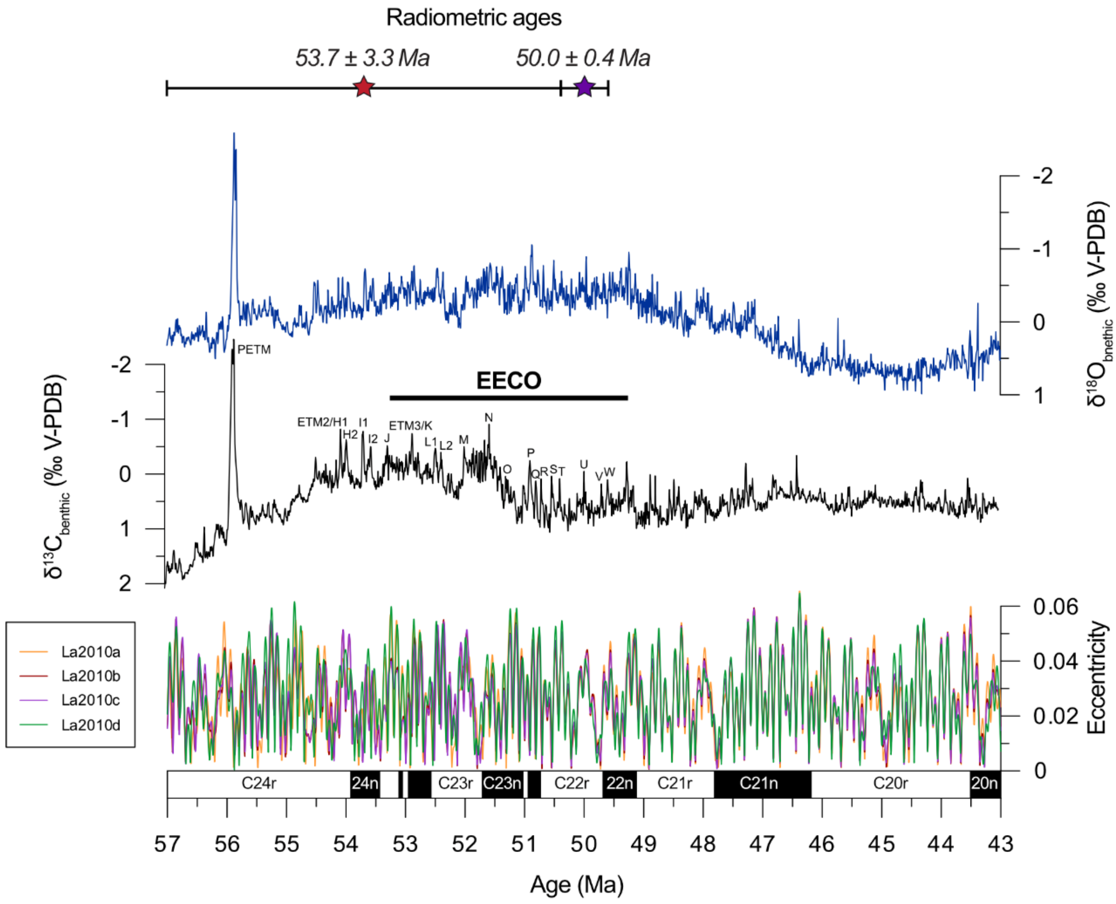

*Extended Data Fig. 8. Timing of Xining CIE compared with CENOGRID and astronomical solutions. CENOGRID showing the evolution of benthic foraminifera stable isotope values[4]. The δ$^{18}$O values show peak warmth of the EECO and the δ$^{13}$C values show several hyperthermal events characterized by negative CIE's. The astronomical solutions[76] show the evolution of the eccentricity of Earth's orbit. The radiometric ages bracketing the CIE in the Xining Basin are indicated.*

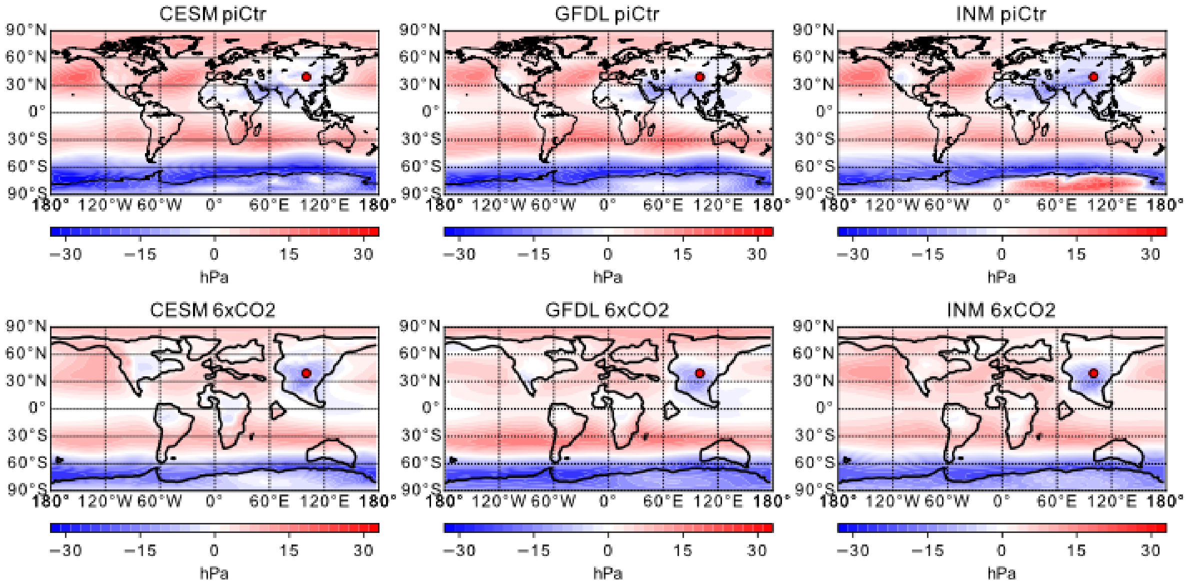

*Extended Data Fig. 9. Summer sea-level atmospheric pressure anomalies in DeepMIP climate model simulations. Sea-level atmospheric pressure anomalies during summer (JJA) in the 6x $pCO_2$ Eocene and the pre-industrial control simulations of the DeepMIP ensemble. Red dot indicates the location of the Xining Basin.*